Contributions to Mineralogy and Petrology (2024) 179:99
https://doi.org/10.1007/s00410-024-02174-5

ORIGINAL PAPER

Spatial and temporal mush heterogeneity during eruptions recorded in clinopyroxene from the 2021 paroxysms at Mt. Etna, Italy

Alice MacDonald[1] · Teresa Ubide[1] · Silvio Mollo[2,3] · Jacopo Taddeucci[3]

Received: 22 February 2024 / Accepted: 15 September 2024

Abstract

Textural and compositional zoning of volcanic minerals archives pre-eruptive magma processes. Crystals erupted simultaneously may be sampled from different regions of the plumbing system and hence record variable histories due to complex magma dynamics. In addition, crystals erupted throughout the course of an eruption may record temporal variations in the plumbing system. To resolve mush variability on both spatial and temporal scales, we investigate clinopyroxene erupted during a series of paroxysmal episodes between February–April 2021 at Mt. Etna, Italy. Using a combination of high-resolution geochemical techniques, we observe that Cr enrichments in clinopyroxene mantle zones, grown upon eruption-triggering mafic rejuvenation, exhibit both temporal and spatial (sample-scale) variability. Temporal variability correlates with changes in glass compositions, attesting to the ability of clinopyroxene to track magma maficity throughout an eruption. Spatial variability, indicated by the scatter of Cr concentrations, is greatest for the first event and lowest for the final paroxysm. In conjunction with core textures, degree of sector enrichment and thermobarometry, our data suggest that the onset of the paroxysms was preceded by the remobilisation of a mid-crustal clinopyroxene mush (534 ± 46 MPa) by hot, mafic magma causing variable resorption of mush-derived crystal cores. Towards the end of the eruption, waning magma supply led to less efficient mush remobolisation and mixing, resulting in homogenous crystal populations. Our results highlight that clinopyroxene Cr contents and sector enrichment can be used to track mafic rejuvenation and magma evolution throughout eruptions, while also reflecting spatial heterogeneities within the plumbing system.

Keywords Mt. Etna · Clinopyroxene · Mush disaggregation · Concentric zoning · Sector zoning

Introduction

Understanding pre-eruptive magma processes is critical in constraining the drivers of volcanism. Mineral compositional zoning and textures provide a means of exploring the dynamics and architecture of plumbing systems (Streck 2008; Kent et al. 2023). However, erupted magmas often entrain crystals with variable thermal histories from different regions of magmatic reservoirs, resulting in sample-scale (i.e., thin section) heterogeneities and in crystal populations that exhibit both spatial and temporal variabilities (Couch et al. 2001; Wallace and Bergantz 2005; Cashman and Blundy 2013; Mangler et al. 2020; Kahl et al. 2023). These heterogeneities may complicate mineral records, yet also reflect the current understanding of many volcanic plumbing systems as vertically extensive crystal-rich mush with ephemeral melt lenses (Cashman et al. 2017; Edmonds et al. 2019). Crystal mushes can be rapidly remobilised and transformed into eruptible magmas by an array of eruption-triggering mechanisms, such as mafic recharge and mafic rejuvenation (where mafic recharge refers to the input of mafic magma into a predominantly felsic systems, and mafic rejuvenation describes the intrustion of mafic magma into a mafic system; Kent et al. 2023). The addition of hotter, more mafic magma leads to the onset of convection and mixing that can lead to eruption (Burgisser and Bergantz 2011; Cooper and Kent 2014; Sparks et al. 2019). The defrosting

Communicated by Ralf Dohmen.

✉ Alice MacDonald
alice.macdonald@uq.edu.au

[1] School of the Environment, The University of Queensland, St Lucia, QLD 4072, Australia

[2] Department of Earth Sciences, Sapienza–University of Rome, P. Le Aldo Moro 5, 00185 Rome, Italy

[3] Istituto Nazionale di Geofisica e Vulcanologia–INGV, Via Di Vigna Murata 605, 00143 Rome, Italy

Published online: 08 October 2024

of a mush system causes crystals to become entrained in the magma, with chaotic mixing resulting in crystal cores recycled from different physiochemical environments (Bergantz et al. 2015; Perugini 2021). Importantly, crystal mantles and rims grown from the magma feeding the eruption can reflect syn-eruptive changes in magma composition that link to changes in eruption style (Gansecki et al. 2019; Ubide et al. 2023). Therefore, linking spatial and temporal controls on syn-eruptive crystal records can provide a powerful tool to unravel syn-eruptive magma dynamics.

Clinopyroxene has been used to infer mush cannibalisation (Di Stefano et al. 2020) and mafic rejuvenation as an eruption trigger (Ubide and Kamber 2018) but the interplay of both effects has not yet been investigated over the course of an eruption. Clinopyroxene is commonly found across a range of volcanic settings, including arcs (Arculus 1978; Di Stefano et al. 2020), mid ocean ridges (Hekinian and Thompson 1976), ocean island basalts (Hammer et al. 2016; Ubide et al. 2023), continental intra-plate volcanoes (Wass 1979; Tapu et al. 2022), and complex tectonic settings like Iceland (Neave and Putirka 2017) and is particularly useful to investigate active volcanoes dominated by mafic, alkaline and volatile-rich compositions where plagioclase records are suppressed by high melt-H_2O content (Giacomoni et al. 2014; Ubide et al. 2022). The stability of clinopyroxene across a range of pressures, temperatures and magma volatile contents in different tectonic settings (Grove and Juster 1989; Blundy et al. 1995; Scaillet et al. 2016; Mollo et al. 2018), the sensitivity of its texture and chemistry to changes in crystallisation conditions (Streck 2008; Putirka 2008; Mollo et al. 2018; Arzilli et al. 2022) and the slow diffusion of cations in its lattice in comparison to other mafic minerals such as olivine (Van Orman et al. 2001; Müller et al. 2013) make it an effective archive of pre-eruptive processes. Concentric zoning in clinopyroxene can be used to track changes in magma composition, with enrichments in Cr indicative of eruption triggering mafic rejuvenation (Ubide and Kamber 2018), while sector zoning reflects dynamic crystallisation pathways modulating magma undercooling (Kouchi et al. 1983; Ubide et al. 2019a, 2019b; Masotta et al. 2020). Clinopyroxene therefore provides exciting potential to better quantify the combined effects of mafic rejuvenation and mush disaggregation in space and time.

Here, we explore spatial and temporal reservoir heterogeneities on the scale of weeks to months, using clinopyroxene from a range of lava, bomb, lapilli, and ash samples erupted during the paroxysmal episodes that occurred between the 16th February–1st April 2021 at Mt. Etna, Italy. As one of the most active and well monitored volcanoes globally, Mt. Etna is an ideal candidate to link changes in mineral chemistry with monitoring signals (e.g., Kahl et al. 2013). Clinopyroxene is stable across a broad range of magma conditions at Mt. Etna, and as an early *liquidus* phase, spans the vertically extensive plumbing system (Armienti et al. 2007; Mollo et al. 2015a, 2015b; Perinelli et al. 2016). Compositional zoning of clinopyroxene erupted at Mt. Etna, including sector and concentric zoning, provides key insights into pre- and syn-eruptive magma histories and dynamics (Mollo et al. 2015b, 2018; Giacomoni et al. 2016; Ubide and Kamber 2018; Ubide et al. 2019a; Magee et al. 2020; MacDonald et al. 2022, 2024). Using a combination of high-resolution geochemical techniques, including laser ablation inductively coupled plasma mass spectrometry and X-ray fluorescence microscopy mapping, we track the spatial and temporal variability of clinopyroxene textural and compositional data to assess how pre-eruptive dynamics evolved over the course of the paroxysms.

Methods

Geological setting and samples

This study investigates a range of lava, bomb, lapilli, and ash trachybasalt samples collected during the February–April 2021 paroxysms at Mt. Etna (11 samples in total; Fig. 1, Table S1). The paroxysmal episodes occurred at the South-East Crater (SEC), located near the summit, and were characterised by Strombolian and lava fountaining activity with short repose times between episodes (Andronico et al. 2021; Corsaro and Miraglia 2022). The 2021 paroxysms

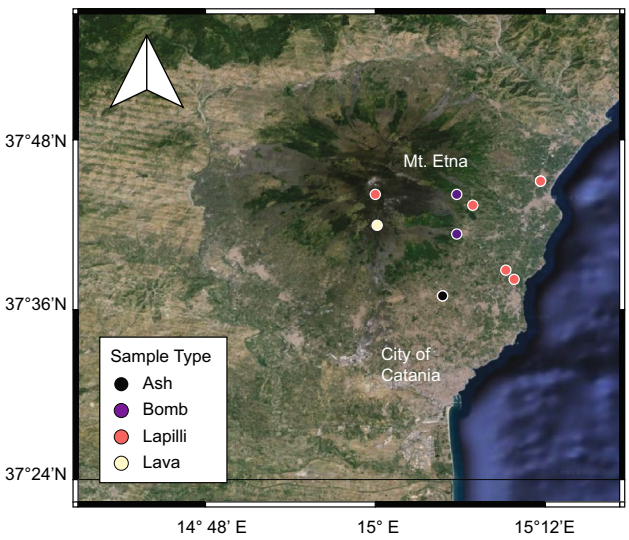

Fig. 1 Locations of samples used in this study on a Google Earth satellite image of Mt. Etna (Italy). Samples represent tephra and lava erupted from 16th February to 23rd March 2021 and collected close to the summit of Mt. Etna (50x samples) and by local citizens from areas distal to the volcano summit (60x samples, Table S1)

are classified as summit eruptions, which are fed by the complex, vertically extensive central conduit plumbing system at Mt. Etna. These contrast with eccentric eruptions which connect deep magma storage at ca. 10 km depth with the surface via dykes that bypass the central conduits of the volcano (e.g., Corsaro et al. 2009; Ubide and Kamber 2018).

Lava and tephra samples named "50x" were collected by the INGV and tephra samples named "60x" were collected by local citizens after each paroxysmal event. Samples are primarily porphyritic (porphyritic index approx. 15%), including phenocrysts (defined as crystals > 400 μm) and microphenocrysts (100–300 μm) of plagioclase, clinopyroxene and olivine and minor amounts of titanomagnetite (as microphenocrysts). The groundmass consists of plagioclase, clinopyroxene, olivine and titanomagnetite microcrysts (< 100 μm) (Fig. 2a).

Analytical methods

Major element compositions of clinopyroxene were acquired using electron probe microanalysis (EPMA) at the Queensland University of Technology Central Analytical Research Facility (CARF), Australia, at The University of Queensland Centre for Microscopy and Microanalysis

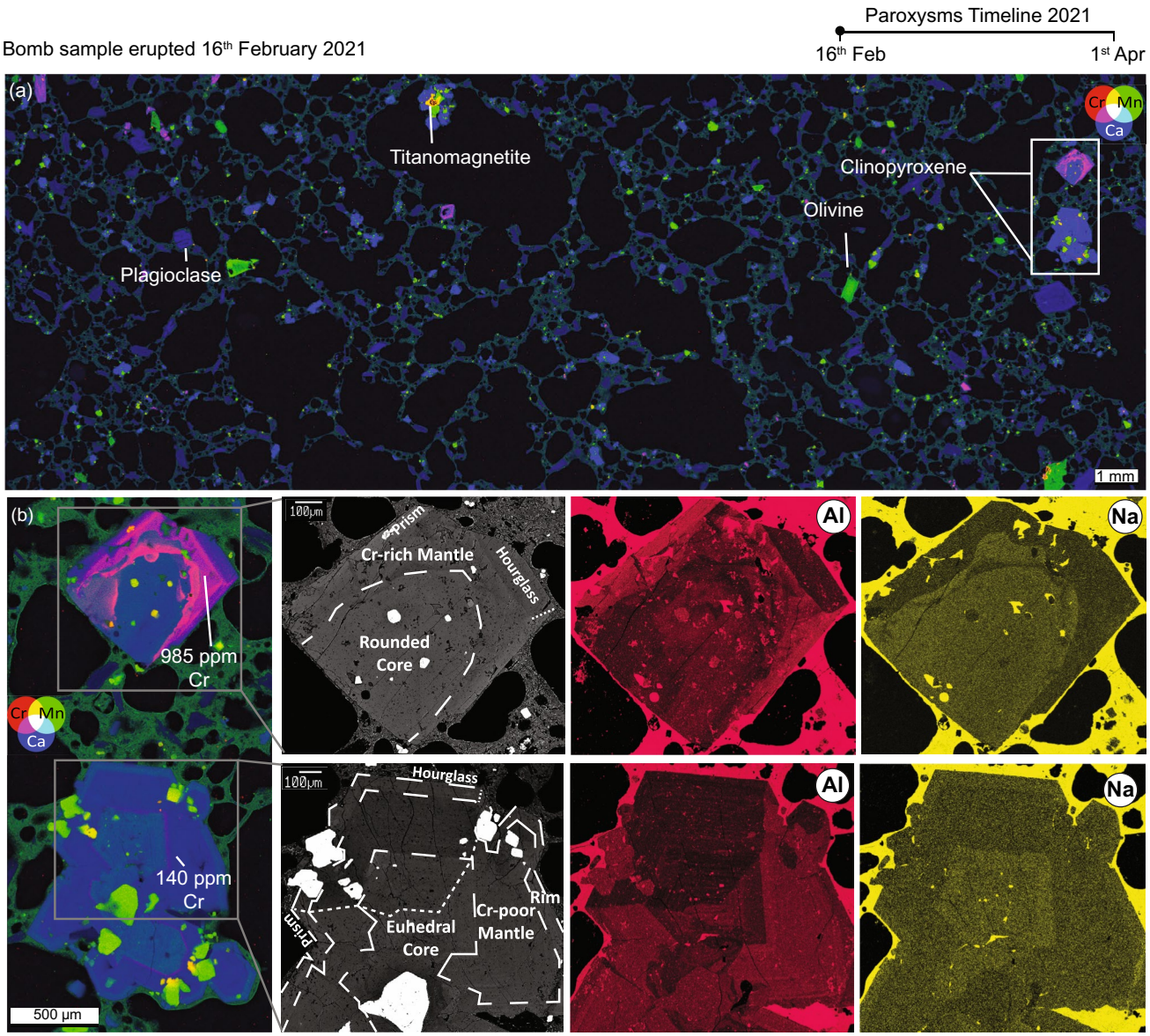

Fig. 2 **a** Three element Synchrotron XFM map (red: Cr, green: Mn, blue: Ca) of the bomb sample erupted during the first paroxysm (16th February 2021); black rounded areas are vesicles. **b** Detailed compositional maps (XFM and FE-SEM) and back-scattered electron (BSE) images of the two crystals located in the white box in (**a**). Clinopyroxene concentric and sector zones are marked in BSE images. FE-SEM images are semi-quantitative, with darker shades of the selected colour representing lower concentrations

(UQ-CMM) and at the HP-HT Laboratory of Experimental Volcanology and Geophysics (HP–HT Lab) of the Istituto Nazionale di Geofisica e Vulcanologia (INGV) in Rome, Italy. Details of analytical conditions used in each laboratory are provided in Table S2.

Analyses conducted at CARF used a JEOL JXA 8530F Hyperprobe equipped with five wavelength dispersive spectrometers. An in-house clinopyroxene standard was routinely measured as a monitor of data quality. Accuracy was better than 3% and precision was better than 4% for all measured elements with respect to the secondary standard (Table S3). Table S3 also includes accepted values for all secondary standards used for EPMA analyses in this study. Precision was also assessed using the EPMA-outputted uncertainty based on counting statistics for both the secondary standard and sample measurements and was typically better than 1% for elements with abundance > 1 wt.% and better than 10% for elements with abundance < 1 wt.% (Table S3, S7).

Analyses at UQ-CMM were collected using a JEOL JXA-8200 microprobe equipped with five wavelength dispersive spectrometers. Kakanui augite, Lake Co feldspar and Springwater olivine (Jarosewich et al. 1980) were routinely analysed to monitor accuracy and precision during the analytical session. Typically, these were better than 3% and 2%, respectively, for elements with abundance > 10 wt.%; 7% and 5% for elements with abundance 1–10 wt.%, and 15% and 8% for elements with abundance < 1 wt.% (Table S3). Analytical precision determined using EPMA-outputted uncertainties based on counting statistics was typically better than 2% for elements with abundance > 10 wt%; 5% for elements with abundance between 1 and 10 wt.% and typically better than 15% for Na_2O (Tables S3, S7).

At the HP-HT Lab, data were collected using a JEOL JXA-8200 equipped with five wavelength dispersive spectrometers MAC augite, albite and orthoclase were used as a quality monitors. Accuracy and precision based on secondary standards were typically better than 1–5% for elements with abundance > 1 wt.%. For elements with abundance < 1 wt.%, accuracy was typically better than 1–10% (Table S3). Precision determined by EPMA-outputted uncertainties was better than 2% for elements with abundance > 1 wt.% and typically better than 10% for elements with abundance < 1 wt.% (Tables S3, S7).

Major and minor element compositional maps of clinopyroxene crystals were produced using a JEOL 6500F field emission-scanning electron microscope (FE-SEM) equipped with an energy-dispersive spectrometer (EDS) at the HP-HT Lab, INGV. X-ray maps were collected using an accelerating voltage of 15 kV, 8 nA probe current and a dwell time of 10 ms per pixel.

Two thin sections from this study (lava sample 503 and tephra sample 502) were selected for X-ray fluorescence microscopy (XFM) mapping at the Australian Synchrotron. The selected samples were representative of the different eruptive products from the paroxysms. To obtain enhanced resolution and precision, maps of relatively light elements including transition metals Cr, Ti, and Mn were acquired at a low energy (7.05 keV) below the Fe$K\alpha$ line following Barnes et al. (2020). Samples were first mapped using a spot size of 5 µm, a scan speed of 10 mm/s and a slit size of 6 µm, scanning the entire thin section. Specific crystals were subsequently mapped at a higher spatial resolution using a reduced size of 1.5 µm and a scan speed of 2 mm/s. The volume fraction of each crystal population was quantified from thin section maps using the colour thresholding function in ImageJ and normalised to account for the volume fraction of vesicles in each sample.

Trace element compositional maps were produced using Laser Ablation Inductively Coupled Mass Spectrometry (LA ICP-MS), following the mapping technique outlined in Ubide et al. (2015). Compared to Synchrotron XFM mapping, which affords high spatial resolution, LA-ICP-MS mapping allows for a greater range of analytes to be measured, including quantification of heavy high field strength elements and rare earth elements. Crystals were selected from those previously analysed by EPMA. Analyses were conducted at The University of Queensland Centre for Geoanalytical Mass Spectrometry, Radiogenic Isotope Facility (UQ RIF-lab). We used an ASI RESOlution 193 nm excimer UV ArF laser ablation system with a dual-volume Laurin Technic ablation cell, operated using GeoStar software. This was used in conjunction with a Thermo iCap RQ quadrupole mass spectrometer, controlled using Qtegra software. Ablation occurred in an environment of ultrapure He, to which trace amounts of Ar and N_2 were added to aid in transport and ionisation of ablated material. Prior to analysis, the instrument was tuned using NIST-612 glass reference material. We used a fluence of 3 Jcm^{-2}, a repetition rate of 10 Hz and a path separation of 1 µm, with different spot sizes, depending on the size of the area of interest. For larger regions, we used a spot size of 20 × 20 µm, a scan speed of 20 μms^{-1}, or a spot size of 16 × 16 µm with a scan speed of 16 μms^{-1}. Smaller crystals were mapped using a spot size of 12 × 12 µm and a scan speed of 12 μms^{-1}. We analysed each crystal twice, using two different analyte menus to maximise precision and spatial resolution on a large number of trace elements, following Ubide et al. (2019a). The first analyte menu included ^{7}Li, ^{23}Na, ^{27}Al, ^{43}Ca, ^{45}Sc, ^{49}Ti, ^{51}V, ^{52}Cr, ^{60}Ni, ^{88}Sr, ^{90}Zr, ^{93}Nb, ^{178}Hf and ^{181}Ta, with a total mass spectrometer sweep time of 147 ms. The second analyte menu included ^{43}Ca, ^{89}Y, ^{139}La, ^{140}Ce, ^{141}Pr, ^{146}Nd, ^{147}Sm, ^{153}Eu, ^{157}Gd, ^{159}Tb, ^{163}Dy, ^{165}Ho, ^{166}Er, ^{169}Tm, ^{172}Yb and ^{175}Lu, with a sweep time of 195 ms. Data reduction was undertaken using Iolite v4 (Paton et al. 2011) in quantitative mode. To quantify

our data, we used CaO obtained by EPMA as the internal standard (22.5 wt. % CaO from 1193 analyses). NIST612 was used as the calibration standard for all analytes except Ti and Cr, for which BHVO-2G glass reference material was used. To monitor data quality, BCR-2G, GSD-1G and BHVO-2G were routinely analysed. Typically, accuracy was better than 10% and precision was better than 5% (Table S4). Trace element concentrations were obtained for individual crystal zones by extracting data from trace element maps using the From Selections option of the Monocle plug-in for Iolite (Petrus et al. 2017). We selected both concentric and sector zones, identified using Cr and Al compositional maps, respectively. We avoided inclusions, cracks, and groundmass crystals by also using semi quantitative Ca compositional maps when selecting regions.

Groundmass major and trace element data were obtained using LA-ICP-MS, following the method of Ubide et al. (2023) and using the same UQ-RIF instrumentation as detailed above. We used 50 µm diameter rasters with a repetition rate of 10 Hz, a fluence of 3 Jcm^{-2} and a scan speed of 5 μms^{-1}. Data reduction was undertaken using Iolite v.4 (Paton et al. 2011) with BCR-2G as the calibration standard. To determine major element compositions, the sum of the major element oxides was normalised to 100% offline. Silicon concentrations determined in this step were used as the internal standard to quantify trace elements for each raster in Iolite. Results were screened for contamination by crystal cargo using Ca-Sc-Cr (clinopyroxene), Al-Sr (plagioclase) and Mg-Ni-Mn (olivine). Accuracy and precision were monitored using BHVO-2G and GSD-1G, and were typically better than 10% and 4%, respectively (Table S5).

Clinopyroxene—melt thermobarometry

Pressure and temperature conditions of crystallisation were estimated for clinopyroxene cores and mantles (identified texturally) by iteratively solving Eq. 33 of Putirka (2008) for T with Equation A of Putirka et al. (2003) for P, using the Thermobar package for python (Wieser et al. 2022; v.1.0.27). This combination of thermobarometric calibrations has previously been identified as a good predictor for mafic alkaline compositions (Mollo et al. 2018) and has been shown to reproduce P–T in crystal cores and sector-zoned mantles formed at low degrees of magma undercooling ($\Delta T = T_{crystallisation} - T_{liquidus}$; MacDonald et al. 2023). We also calculate P–T using the random forest machine learning clinopyroxene-melt model of Jorgenson et al. (2022), which has also been shown to be suitable for clinopyroxene crystallising at a range of ΔT (MacDonald et al. 2023). We propagate EPMA-outputted uncertainties using Thermobar (Wieser et al. 2022) to estimate the errors associated with each calculated P–T. For the melt composition, we used the average groundmass compositions of the entire data set determined using LA-ICP-MS of a lava sample (Table S6). For clinopyroxene cores, we tested a more evolved glass composition from the 2021 paroxysms obtained by Corsaro and Miraglia (2022) to compare with results obtained using our groundmass composition.

To test for clinopyroxene-melt equilibrium, we used a range of equilibrium models which compare measured clinopyroxene components with those predicted from melt compositions (Mollo et al. 2013b; Putirka 1999): DiHd (± 0.1 ΔDiHd), EnFs (± 0.05 ΔEnFs), CaTs (± 0.06 ΔCaTs) and CaTi (± 0.02 ΔCaTi). In each case, if the difference between the measured and predicted compositions (Δ) is less than the threshold value, chemical equilibrium between the clinopyroxene and chosen melt composition is considered achieved. For sector-zoned clinopyroxene, the combination of these models has been experimentally demonstrated as to be an effective test for clinopyroxene-melt equilibrium, avoiding the issues which plague the Fe–Mg exchange model (MacDonald et al. 2023).

Results

Clinopyroxene textural variability

Clinopyroxene is the second most abundant mineral phase in our samples (~ 7 vol.% on a vesicle free basis, as determined from ImageJ analysis on Synchrotron XFM compositional maps from two samples), following plagioclase as the most abundant (~ 17 vol.%), typical of central conduit products from Mt. Etna (e.g., Corsaro et al. 2009; Magee et al. 2021).

Thin section scale XFM maps, in addition to detailed XFM, LA-ICP-MS and FE-SEM maps of individual crystals, highlight the variability in clinopyroxene textures (Figs. 2 and S1). Based on textural observations, compositional maps and EPMA data, clinopyroxene can be split into three main concentric zones: cores (which may be euhedral or rounded), mantles (euhedral), and rims (euhedral; Figs. 2b, 3). In addition to this, crystals are also commonly sector-zoned, with Al-rich prism and Al-poor hourglass sectors, typical of low degrees of magma undercooling and sluggish crystallisation kinetics at Mt. Etna (Ubide et al. 2019a; Masotta et al. 2020; MacDonald et al. 2022). Mantles and rims are almost always sector-zoned, while cores are observed both with and without sector zoning (Fig. 2b). Within a single thin section, cores may either be strongly rounded or euhedral. The texture of cores appears to be related to the compositional contrast with subsequent mantles, with rounded cores typically accompanied by mantles with Cr > 500 ppm. Mantles with moderate Cr

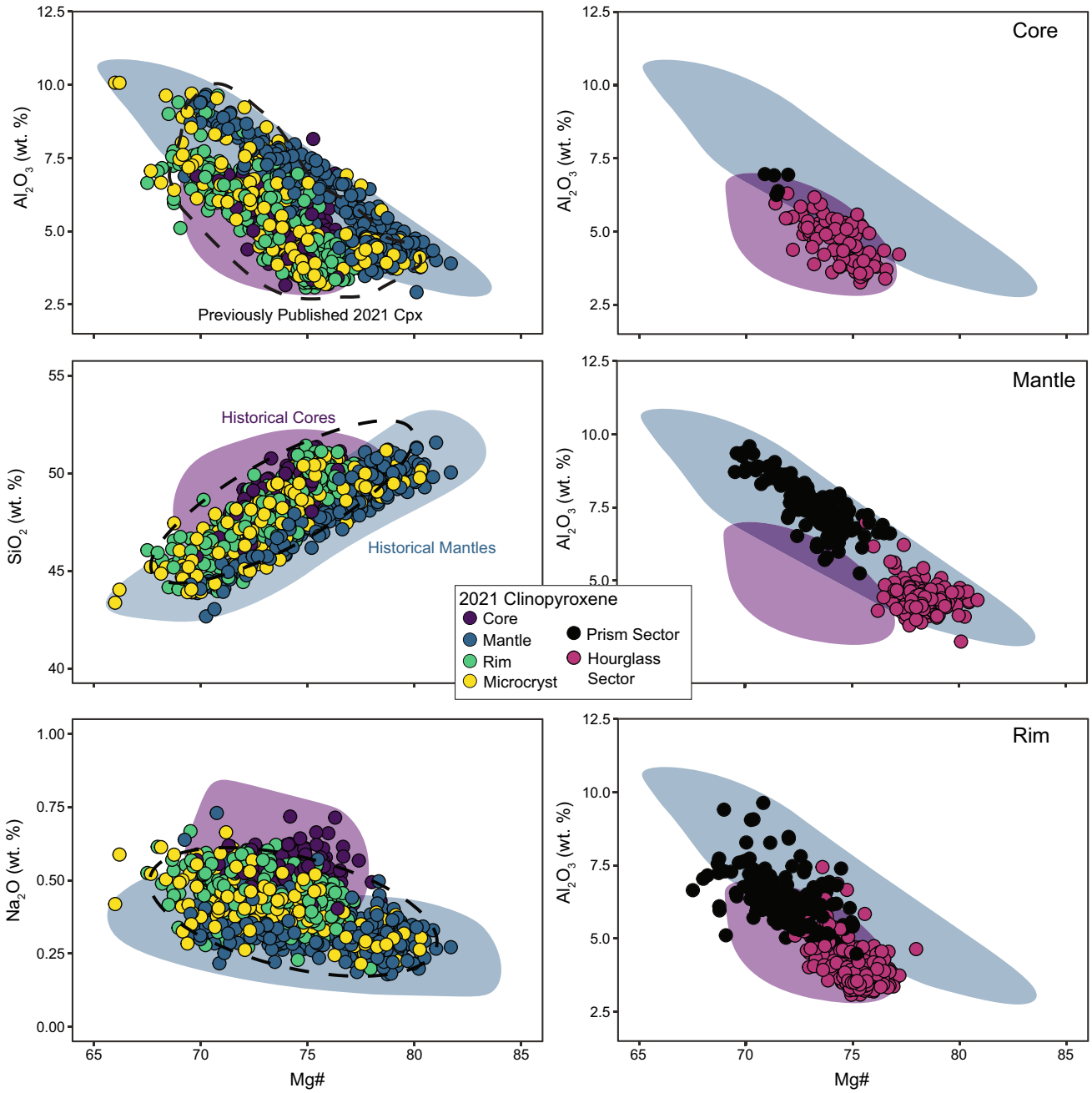

Fig. 3 Major and minor element compositions of clinopyroxene crystals from the 2021 paroxysms, plotted against Mg# (Mg# = MgO/(FeO_t + MgO) × 100 on molar basis). Panels on the left are coloured by concentric zone, whereas panels on the right are for Al_2O_3 only, and they are coloured by sector zone and separated into panels by concentric zone. Historical data are from the compilation reported in MacDonald et al., (2024) and include data from the 1974 eccentric eruption (Ubide and Kamber 2018; Ubide et al. 2019a), the 1669 central conduit flank eruption (MacDonald et al. 2024) and the 2002–03 eccentric eruption (Ubide et al. 2019a). Dashed regions indicate previously published data from the 2021 paroxysms (Mollo et al. 2022; Musu et al. 2023), excluding outliers. EPMA-outputted uncertainties are smaller than the symbols

concentrations (Cr = 100–500 ppm) encapsulate rounded cores which are typically not as resorbed. Euhedral cores are usually rimmed by mantles with Cr-poor bands (Cr < 150 ppm; Fig. 2b).

Major element compositions

Clinopyroxene cores, mantles and rims have broadly similar major element compositions, yet define slightly distinct groups in bivariate plots against Mg# (Mg# = Mg/(Mg + Fe_t) × 100 on molar basis; Fig. 3).

Mantle zones typically have the highest Mg# and Al_2O_3 and lowest SiO_2 and Na_2O compositions compared to cores, rims and microcrysts (Fig. 3, Table 1). Cores have the highest Na_2O, followed by rims and mantles (Table 1). Across our set of samples, clinopyroxene crystals from different sample types and erupted at different dates define similar geochemical trends (Fig. S2). Our data are similar to previously published 2021 clinopyroxene data (see dashed regions in Fig. 3; Mollo et al. 2022; Musu et al. 2023) and to texturally constrained clinopyroxene compositions from historical eruptions at Mt. Etna (Ubide et al. 2019a; MacDonald et al. 2024; Fig. 3).

To assess whether concentric zones defined here differ from each other compositionally in a statistically significant manner, we performed the Mann–Whitney *U* statistical test (Nachar 2008) for rounded cores, euhedral cores, mantles, and rims (Table 2). Using Mg#, Na_2O and CaO, our results indicate that cores, mantles, and rims have median compositions which significantly differ from one another ($p < 0.05$). In contrast, rounded and euhedral cores have *p*-values > 0.05. Hence, although they differ texturally, rounded, and euhedral cores are compositionally indistinguishable.

Hourglass sectors are depleted in Al_2O_3 and enriched in MgO relative to prism sectors (Fig. 3, Table S7). Hourglass sectors of core and mantle concentric zones have similar Al_2O_3 compositions, and hourglass sectors in rims have the lowest concentrations of Al_2O_3 (Table 1). In contrast, prism sectors have distinct Al_2O_3 compositions amongst different concentric zones. Prism mantles typically have the highest Al_2O_3 concentrations, followed by prism cores and finally, prism rims (Table 1). These textural constraints highlight that geochemical variations in bivariate plots are largely due to sector zoning (Fig. 3, right panels). Na_2O exhibits little variability between sectors (Fig. 3b), indicating that sector zoning in clinopyroxenes erupted in the 2021 paroxysms follows typical sector zoning in mafic alkaline settings like Mt. Etna (Ubide et al. 2019a; Mollo et al. 2020; Masotta et al. 2020).

Table 2 Results for the Mann–Whitney *U* test to determine if mantles, cores, and rims have statistically distinct compositions. p-values < 0.05 indicate that the compared zones are compositionally distinct

Concentric Zones	Mg# *p*-value	Na_2O *p*-value	CaO *p*-value
Core—mantle	2.34×10^{-10}	$< 2.2 \times 10^{-16}$	$< 2.2 \times 10^{-16}$
Mantle—Rim	$< 2.2 \times 10^{-16}$	$< 2.2 \times 10^{-16}$	$< 2.2 \times 10^{-16}$
Core—Rim	0.0005	$< 2.2 \times 10^{-16}$	0.037
Rounded core—Euhedral core	0.057	0.53	0.21

Trace element compositions

Trace element variations closely follow our textural classifications as defined by back scattered electron images (BSE; Figs. 2b and 4). In general, cores and rims are enriched in high field strength elements (HFSE) and rare earth elements (REE) relative to mantle zones, which are associated with enrichments in Cr (Figs. 4, 5, Table S8). Specifically, cores contain the highest concentration of REE (e.g., $^{Core}Ce = 44 \pm 4$ ppm for hourglass sectors) and HFSE (e.g., $^{Core}Zr = 121 \pm 5$ ppm for hourglass sectors), followed by rims (e.g., $^{Rim}Ce = 34 \pm 4$ ppm, $^{Rim}Zr = 103 \pm 16$ ppm for hourglass sectors) and mantles (e.g., $^{Mantle}Ce = 22 \pm 6$ ppm, $^{Mantle}Zr = 78 \pm 13$ ppm for hourglass sectors). Both rounded and euhedral cores are enriched in REE and HFSE, attesting to their compositional similarity as outlined previously. Core, mantle, and rim concentric zones have similar REE normalised patterns to clinopyroxene erupted from the 1974 and 2002–03 eruptions at Mt. Etna (Fig. 5).

Table 1 Compositions for clinopyroxene zones described in this study. Average values are reported with 1 σ. Note that some cores are not sector-zoned, whereas mantles and rims are typically sector-zoned

Concentric Zone	Sector Zone	Mg#	Al_2O_3 (wt. %)	SiO_2 (wt.%)	Na_2O (wt. %)
Rim	Hourglass	75 ± 1	4.1 ± 0.7	49.6 ± 0.8	0.42 ± 0.06
	Prism	72 ± 2	6.3 ± 0.9	47 ± 1	0.48 ± 0.07
Mantle	Hourglass	78 ± 1	4.5 ± 0.6	49.8 ± 0.7	0.3 ± 0.06
	Prism	73 ± 1	7.5 ± 0.8	46.5 ± 1.1	0.35 ± 0.06
Core	Hourglass	74 ± 1	4.7 ± 0.7	49.6 ± 0.8	0.51 ± 0.06
	Prism	71 ± 0.4	6.7 ± 0.3	47 ± 0.3	0.52 ± 0.06
	Not sector-zoned	75 ± 2	5.2 ± 0.9	48.9 ± 1.1	0.53 ± 0.07

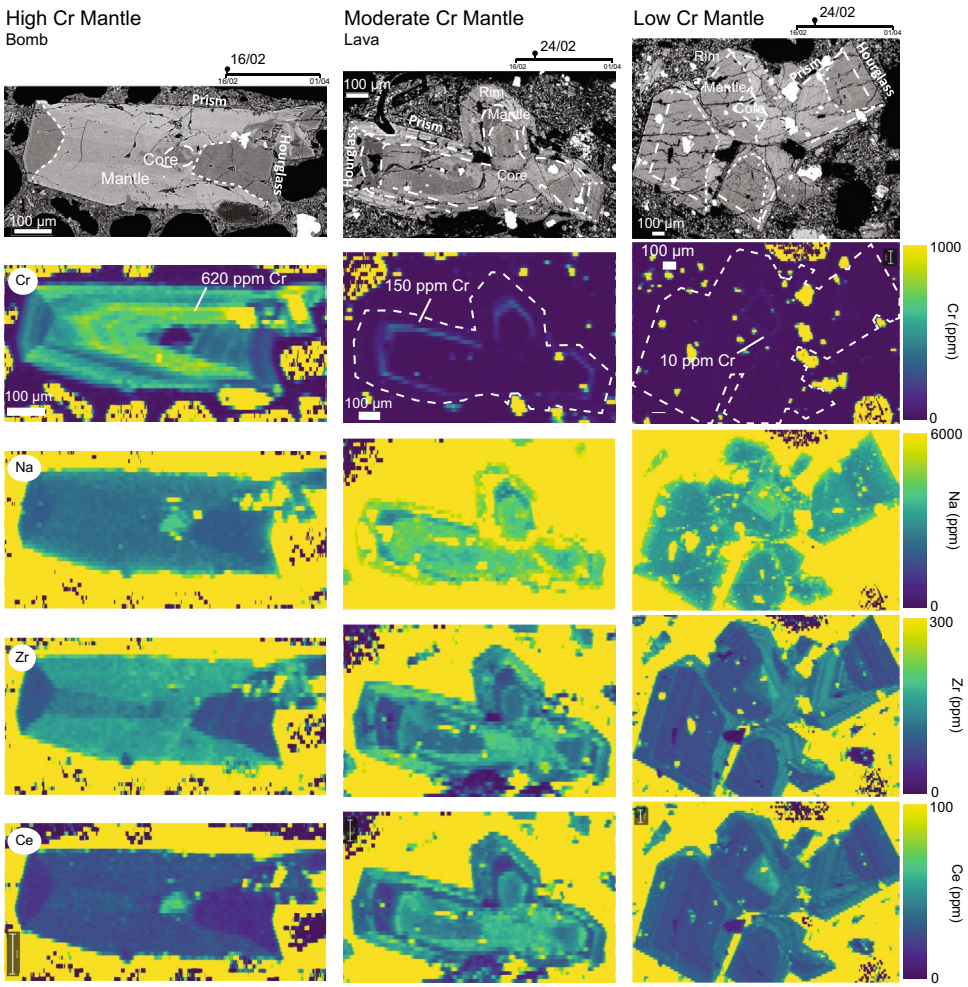

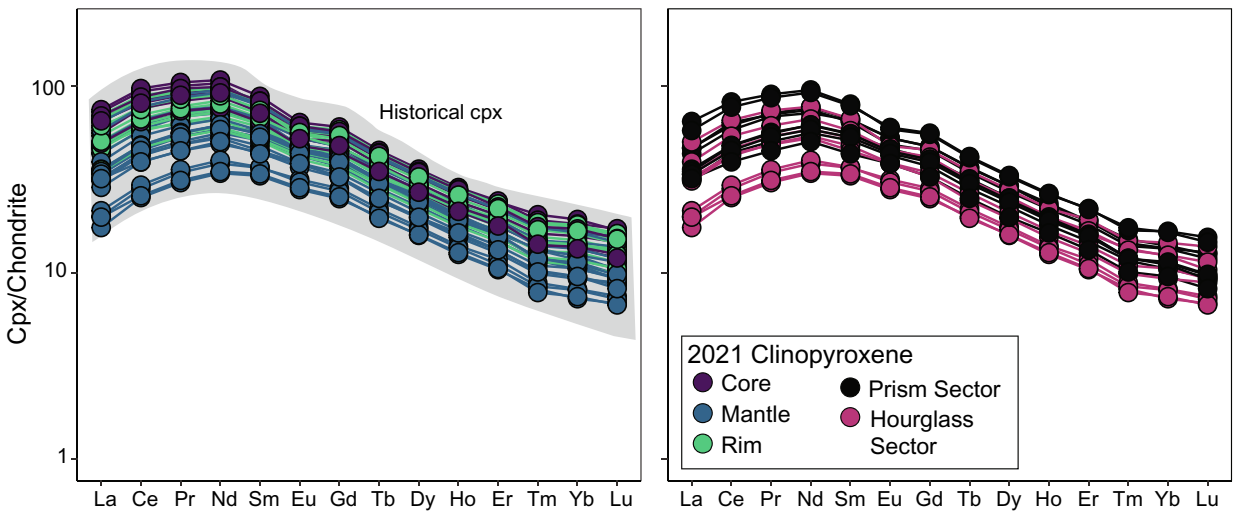

Fig. 4 LA-ICP-MS compositional maps and BSE images of clinopyroxene crystals with varying Cr enrichment in mantle zones. Zones are marked in BSE images, and crystal boundaries are outlined in Cr maps with low Cr rims. Maps are quantitative for clinopyroxene and semi-quantitative for the groundmass

Fig. 5 Chondrite-normalised (McDonough and Sun 1995) clinopyroxene rare earth element (REE) compositions. Data are coloured by concentric zone (left) or sector zone (right). The right panel includes data from all concentric zones (i.e., cores, mantles, and rims). The grey field (left panel) represents clinopyroxene data from the 1974 and 2002–03 eruptions at Mt. Etna from Ubide et al. (2019a)

LA-ICP-MS compositional maps visualise the high variability of Cr enrichment associated with mantles in clinopyroxene crystals across our sample set. As previously highlighted from Synchrotron XFM composition maps on selected samples, the concentration and style of Cr enrichment can vary significantly between crystals from the same sample, with core texture varying with Cr enrichment of mantles (Figs. 4, S1).

Hourglass sectors in all concentric zone types have lower concentrations of REE and HFSE than prism sectors within the same zone (Fig. 5), typical of sector zoning at Mt. Etna and other mafic alkaline systems, where the distribution of trace cations between sectors is controlled by charge-balancing mechanisms associated with the replacement of Si (^{T}Si) by Al (^{T}Al) in the tetrahedral lattice site (Ubide et al. 2019a, 2019b; Masotta et al. 2020; MacDonald et al. 2022). Increasing ^{T}Al causes the probability of REE entering a charge-balanced site to increase (Blundy et al. 1998; Hill et al. 2000; Wood and Blundy 2001; Mollo et al. 2013a, 2020b). Hence, prism sectors, which are enriched in ^{T}Al relative to their hourglass counterparts, accommodate REE more easily into the crystal lattice, in accordance with the exchange reaction (MacDonald et al. 2022):

$$[Di]_{\{-111\}} \leftrightarrow [HFSETs + REETs]_{\{h\,k\,0\}}$$

where Di ($CaMgSi_2O_6$) and *Ts* ($CaAl_2SiO_6 + CaFeSiAlO_6$) components indicate the major cation distributions in clinopyroxene lattice sites.

Clinopyroxene-melt equilibrium and thermobarometry

Of the 556 core and mantle compositions reported in this study, 305 were found to have attained equilibrium with the chosen groundmass composition (Fig. S3). Most compositions fall within equilibrium when considering DiHd, EnFs and CaTs models, but some fail the CaTi test (Fig. S3). This combination of four equilibrium models accounts for both fast (Mg and Ca; DiHd and EnFs) and slow (Al and Ti; CaTs and CaTi) diffusing species in the melt (Zhang et al. 2010). The latter are therefore more sensitive to the development of distinct crystal interface melts, arising from ΔT and crystallisation kinetics associated with sector zoning, which may not be adequately represented by a bulk melt composition (MacDonald et al. 2023). Although the formation of sector zoning is attributed to kinetic effects, in the case of Mt. Etna and other mafic alkaline systems, its occurrence is typically associated with near-equilibrium growth conditions suitable for thermobarometric calculations, as highlighted in previous experimental and natural studies (Kouchi 1983; Ubide et al. 2019a, b). Hereon, we only use compositions which

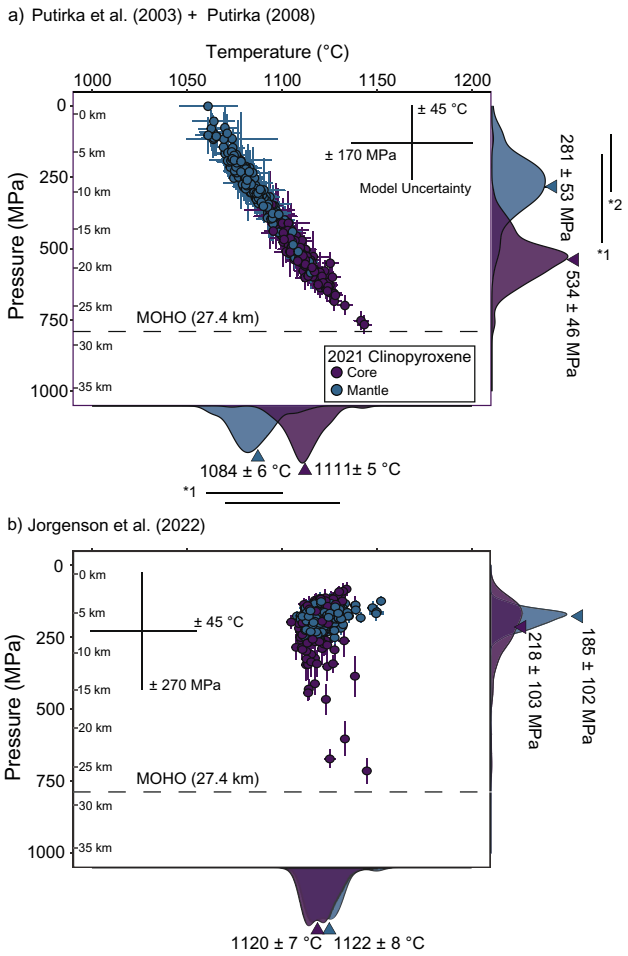

Fig. 6 **a** Estimates of crystallisation *P–T* conditions for clinopyroxene core and mantle zones, calculated following the procedure outlined by MacDonald et al. (2023), obtained by iteratively solving Eq. 33 of Putirka (2008) for T and Equation A of Putirka et al. (2003) for *P*. Bars on the right represent *P–T* estimates from previously published studies of clinopyroxene from the 2021 Etna paroxysms. 1*: Mollo et al. (2022) 2*: Musu et al. (2023) **b** Estimates of *P–T* obtained using the random trees machine learning model of Jorgenson et al. (2022). Conversion of pressure to depth followed the crustal density model of Corsaro and Pompilio (2004). MOHO depth is from Hirn et al. (1997). Error bars on symbols represent uncertainties propagated from EPMA-outputted uncertainties and error bars on plot represent reported calibration uncertainties

indicate attainment of equilibrium following all four models when considering crystallisation *P–T* conditions.

Clinopyroxene and melt compositions obtained in this study were compared to the calibration data set used in Putirka (2008) and Jorgenson et al. (2022). Our clinopyroxene and melt compositions fall within the compositions used to calibrate both models (Fig. S4).

P–T results obtained by applying the Putirka models produce a linear array (Fig. 6a), which is consistent with the thermodynamic principles which underpin the thermobarometers used here. These models are based

on changes in enthalpy, entropy and volume associated with the *T* sensitive diopside-hedenbergite and jadeite clinopyroxene-melt exchange equilibria and with the *P* sensitive incorporation of jadeite in clinopyroxene (Putirka 2008). The thermodynamic formulation of these equilibria results in the calculation of a temperature dependent *P*, and a pressure dependent *T*. In detail, this interdependency arises from the equilibrium condition between solid and liquid phases during the fusion (melting) reaction of most minerals. At higher *P*, the temperature of fusion increases as the denser solid phase, which occupies less space and has a smaller volume relative to the liquid phase, becomes more stable. Consequently, more thermal energy, in the form of higher *T*, is required to facilitate the transition from solid to liquid, leading to an increase in the melting temperature with pressure. Hence, thermobarometers based on thermodynamic principles will predict higher *T* as *P* increases. In contrast, results obtained using the random trees machine learning model of Jorgenson et al., (2022), do not form the same *P*–*T* trends, as this model is not based on thermodynamic principles (Fig. 6b). Moreover, propagated uncertainties from analytical errors are small and do not account for the observed variations (Fig. 6).

Using the Putirka models, cores return the highest average *P* (534 ± 46 MPa; Fig. 6a; reported as average ± standard deviation, model calibration SEE = 170 MPa) and hottest *T* (1115 ± 5 °C, model SEE = 45 °C), indicative of dominant clinopyroxene crystallisation at depth (e.g., Armienti et al. 2007; Giacomoni et al. 2016; Ubide and Kamber 2018; Mollo et al. 2020b). Mantles are associated with shallower crystallisation conditions (281 ± 53 MPa, Fig. 6a), corresponding to crystallisation at ~ 10 km depth, consistent with the main region of magma storage at Mt. Etna at the transition in basement lithology from granitoids to carbonates (Murru et al. 1999; Corsaro and Pompilio 2004; Ubide and Kamber 2018). We note that calculated *P* of cores and mantles have some degree of overlap when the model uncertainty is accounted for, however the resorbed core textures agree with partial dissolution upon upward transport by an intruding mafic melt. Calculated *T* for mantles zones (1084 ± 6 °C) are lower than cores (1111 ± 5 °C), despite mantle enrichment in compatible elements such as Cr which is typically associated with crystallisation from hot, primitive magmas (e.g., Ubide and Kamber 2018). This is partly due to the use of the same melt composition (rock groundmass) for both cores and mantles, which has a strong control on the calculation of *T* using clinopyroxene-melt thermometers (Putirka 2008). We tested pairing the cores with an evolved glass from the eruption (Corsaro and Miraglia 2022) instead of the matrix, and obtained lower *T* for the cores (1098 ± 9 °C; Fig. S5), within error of the mantle *T*. For comparison, we also calculated crystallisation *P*–*T* of mantles using the most mafic glass composition from Corsaro and Miraglia (2022), which returns an almost identical crystallisation *T* (1083 ± 11 °C) compared to results obtained using our groundmass composition. This suggests that the groundmass composition is a reasonable approximation for the melt for the application of clinopyroxene-melt thermobarometry to Cr-rich mantle zones, as previously suggested by Ubide et al. (2023).

In comparison, *P* calculated using Jorgenson et al. (2022) for clinopyroxene cores are very similar (218 ± 103 MPa) to mantles (185 ± 102 MPa), suggestive of clinopyroxene crystallisation restricted to the upper 10 km of the plumbing system (Fig. 6b). Calculated *T* are very similar between zones (1120 ± 7 °C for cores and 1122 ± 8 °C for mantles) and within the reported model uncertainty of ± 45 °C. As for the Putirka models, we tested pairing the cores with an evolved glass from the eruption (Corsaro and Miraglia 2022), which also results in a lower *T* for the cores (1090 ± 5 °C, Fig. S5), but still within model uncertainty of calculated *T* for mantles.

At Mt. Etna, phenocryst rims and groundmass microcrysts with enrichments in Al + Ti relative to Cr-rich mantles are strongly associated with crystallisation upon ascent and decompression, and hence higher ΔT (Mollo et al. 2010; Ubide and Kamber 2018). Increased cooling rates and ΔT result in significant *P*–*T* overestimations due to the disequilibrium uptake of Al and Na cations into microcrysts and rims, with even relatively small cooling rates (e.g., 0.5 °C/min) causing significant overestimates of pressure (Mollo et al. 2010). Rims in clinopyroxene crystals from the 2021 paroxysms are enriched in Al + Ti, REE and HFSE relative to mantle zones, and therefore, we do not include these in our assessment of *P*–*T* crystallisation conditions. Overall, thermobarometry indicates deep crystallisation of clinopyroxene cores, remobilised by mafic magma which crystallised into Cr-rich mantles in the main region of magma storage in the middle crust.

Discussion

Magmatic processes and crystallisation conditions recorded in clinopyroxene zones

Clinopyroxene crystals erupted during the 2021 paroxysms contain three concentric zones; (1) cores, (2) mantles and (3) rims, which may be further subdivided by the presence of sector zoning (prism and hourglass sectors, Table 1). Here, we discuss the potential origins of each of these zones, including crystallisation temperature and pressures, to constrain pre-eruptive magmatic processes in the lead up to the 2021 paroxysmal events.

Overall, clinopyroxene cores, mantles, and rims exhibit parallel normalised REE patterns, indicative of crystallisation from cogenetic melts (e.g., Batki et al. 2018; Li et al. 2020; Tapu et al. 2022; Fig. 5). The depletion of REE in mantles, and higher Mg# and Cr enrichments relative to cores and rims (Figs. 3, 4) attest to the crystallisation of mantles from a more mafic melt, during eruption-triggering mafic rejuvenation (e.g., Ubide and Kamber 2018).

Clinopyroxene-melt thermobarometry provides a means to explore the crystallisation conditions associated with distinct clinopyroxene zones. Our results overlap with previous estimates for the 2021 paroxysms (Mollo et al. 2022; Musu et al. 2023), yet our data suggest the development of deeper mush zones from which clinopyroxene cores were sampled (Fig. 6). We note that the textural classifications in our study differ from those of Mollo et al. (2022) and Musu et al. (2023), however our compositional data set broadly overlaps with these studies (Fig. 3) and thus the difference may lie in the choice of thermobarometric model.

Calculated T for our crystals and those in previous studies broadly overlap and so we focus here on calculated P. Mollo et al. (2022) used a thermobarometer specifically designed for mafic alkaline magmas (Mollo et al. 2018), which may underestimate crystallisation P for clinopyroxene crystallised under very low ΔT at $P \geq 400$ MPa (MacDonald et al. 2023). In contrast, crystallisation conditions reported in Musu et al. (2023) were estimated using random forest thermobarometry (Jorgenson et al. 2022), which we reproduce using our sample set (Fig. 6b, Table S10). Using the data set of this study, this model gives typical crystallisation $P = 100$–300 MPa for both cores and mantles, indicative of shallow crystallisation in the upper 10 km of the plumbing system. We note that the calibration data set of Jorgenson et al. (2022) is consistent with our clinopyroxene and chosen melt compositions, indicating that this is unlikely to be the cause of the discrepancy (Fig. S4).

Importantly, this region is dominated by degassing-driven plagioclase crystallisation at Mt. Etna, suppressed in deeper portions of the plumbing system by the increasing solubility of H_2O in the melt phase (Métrich and Rutherford 1998; Giacomoni et al. 2014; Mollo et al. 2015a, b). Clinopyroxene cores, mantles and rims have small Eu negative anomalies (Fig. 5, Table S9), suggestive of only minor plagioclase crystallisation prior to the growth of each zone, and therefore deeper crystallisation of clinopyroxene than calculated using the Jorgenson et al. (2022) model. To quantify the role of plagioclase fractionation on clinopyroxene rare earth element patterns, we model the extent of plagioclase removal required to produce a melt from which clinopyroxene with the incipient Eu negative anomalies crystallised. We use clinopyroxene-melt partition coefficients for Mt. Etna reported by D'Orazio et al. (1998) to model the composition of the melt in equilibrium with a representative clinopyroxene mantle composition, as well as a hypothetical composition with the same REE pattern but no Eu anomaly (Fig. S6, Table S9). We focus on mantles as the partition coefficients presented in D'Orazio et al. (1998) are from a very primitive Etna erupted composition (VB-72). In addition, to avoid complications which may arise from sector zoning, we chose a mantle composition with no obvious sector zoning. Then, the amount of plagioclase fractionation required to reproduce a melt in equilibrium with clinopyroxene with the Eu anomaly observed in the mantle composition (Fig. S6) was modelled using plagioclase-melt partition coefficients for Mt. Etna (D'Orazio et al. 1998) with the Rayleigh fractional crystallisation equation:

$$C_l = C_0 F^{(D-1)}$$

where C_l is the concentration of Eu in the residual melt, C_0 is the starting composition, F is the fraction of melt remaining and D is the mineral-melt partition coefficient. Results indicate that the crystallisation of clinopyroxene mantles is associated with no more than 5% plagioclase removal (Table S11), lower than the 17% plagioclase observed in our samples. This supports the notion that these zones crystallised prior to plagioclase entering the crystallisation assemblage as a major phase in the plumbing system. In addition to this, correlation matrices evaluating the influence of clinopyroxene composition on P calculated using the model of Jorgenson et al. (2022) show that pressure changes are weakly dependent on the compositional evolution of clinopyroxene (Fig. S4). In contrast, P calculated using the model of Putirka et al. (2003) strongly responds to the equilibrium partitioning of Na between clinopyroxene and melt, thus resulting in a more effective P-dependent reaction due to the notable change in molar volume caused by the solution of jadeite in mineral solid solution (Nimis 1995; Fig. S4b). Hence, we favor the results obtained from the Putirka et al. (2003) model (Fig. 6a), which we use to discuss magmatic architecture and crystallisation conditions henceforth.

Exploring each zone in detail, clinopyroxene cores correspond to the deepest crystallisation conditions, indicated by thermobarometry results (Fig. 6a) and elevated Na contents relative to later forming mantle zones (Fig. 3, Table 1). Crystallisation of REE rich clinopyroxene cores such as the ones in this study can be attributed to either (1) crystallisation from a relatively evolved trachybasaltic melt or (2) the effect of increased Na (and hence, jadeite component) in cores at depth which overwhelms the effect of ^{T}Al on the incorporation of REE (Mollo et al. 2020a). In the latter case, deep clinopyroxene cores at Mt. Etna are anticipated to have high Mg# relative to zones associated

with shallower crystallisation and record *P* conditions closer to 750–950 MPa (Mollo et al. 2020a). However, in crystals from the 2021 paroxysms, cores have lower Mg# than mantles, and record shallower crystallisation *P* than those from the study of Mollo et al. (2020a). Hence, we attribute the enrichment of REE to crystallisation of clinopyroxene cores from a relatively evolved melt at shallower pressures than those of Mollo et al. (2020a). Due to the high magma fluxes buffering magma compositions to trachybasalts at Mt. Etna, we infer that this evolved melt likely does not differ greatly from the intruding magma. The mixing of magmas which are only discretely different has previously been suggested to be sufficient to trigger mush remobilisation in Icelandic systems (Neave et al. 2021), supporting this possibility. The presence of sector zoning in some cores attests to magma dynamics associated with low ΔT (< 45 °C; Kouchi et al. 1983; Masotta et al. 2020; MacDonald et al. 2022; Mollo et al. 2023). However, not all cores exhibit observable sector zoning (Fig. 2b), suggesting core formation also occurred at very low ΔT (approaching zero), attesting to variable thermal conditions that may also control the incorporation of REE and HFSE in agreement with the positive enthalpy and entropy of fusion of common igneous minerals (Wood and Blundy 2001).

The variable degrees of resorption of cores suggests the intrusion of hotter and more mafic magma leading to subsequent crystallisation of mantle zones (e.g., Ubide and Kamber 2018; Fig. 2b). Thermobarometry results using both groundmass and glass compositions indicate that crystallisation *T* of cores is higher, but within model uncertainty, of mantle zones and consistent with crystallisation at higher *P* (Fig. 6a, S4). For comparison, we also consider *T* using differing melt compositions using the Jorgenson et al. (2022) model. Although, as discussed earlier, *P* calculated using this model are low and not consistent with our textural observations and Eu anomalies, *P* and *T* are not calculated iteratively and are not as strongly dependent on one another, allowing us to independently consider estimates of crystallisation *T*. Cores have slightly cooler crystallisation *T* (1090 ± 6 °C) than mantles (1122 ± 7 °C), however both are also within the reported model uncertainty (± 45 °C; Fig. S5). If accurate, these results indicate that the crystallisation of cores occurred at similar *T* to mantles, and that resorption was induced by subtle differences in magma composition and *T* which are not resolvable using currently available clinopyroxene-melt thermometers.

Mantles represent a phase of shallower crystallisation and are markedly mafic relative to the cores they encapsulate, with variable enrichments in Cr. Their relative depletion in HFSE and REE relative to cores and higher Mg# are highly suggestive of crystallisation by mafic rejuvenation, which may trigger volcanic eruptions (Ubide and Kamber 2018). Sector zoning is also present in all analysed clinopyroxene mantles, indicative of dynamic crystallisation under low ΔT (Ubide et al. 2019a) which could be induced by magma mixing and incipient mush remobilisation.

Finally, clinopyroxene rims are Cr-poor compared to mantles (Fig. 4) and have major and trace element compositions intermediate between cores and mantles (Figs. 3 and 5). Cr-poor clinopyroxene rims at Mt. Etna are typically interpreted to record decompression-induced crystallisation during magma ascent, attributed to their higher concentrations of Al and lower concentrations of Mg relative to Cr-rich mantles (Mollo et al. 2010, 2013a, b; Ubide and Kamber 2018). In our samples, the contrast in Al (and Ti) between Cr-poor rims and Cr-rich mantles is not as distinct as previous eruptions (Fig. 2b; Ubide and Kamber 2018), with major element compositions and REE concentrations that lie between those of cores and mantles (Figs. 3 and 5). In addition, limited Eu anomalies (Fig. 5) discount the coeval formation of significant proportions of plagioclase. Altogether, these observations suggest that rim crystallisation occurred during initial stages of magma ascent following mafic rejuvenation, but prior to plagioclase crystallisation in the shallow plumbing system. Hence, for the 2021 paroxysms the rims may not capture the full ascent pathway and instead formed during the initial stages of ascent.

Cr in clinopyroxene: Temporal heterogeneity

Clinopyroxene cores, mantles, and rims each represent distinct phases of crystallisation throughout the vertically extensive plumbing system at Mt. Etna. A critical observation arising from the consideration of these zones is that the texture of cores and the Cr concentration of mantles varies considerably both on the sample scale and between different paroxysms. In mafic alkaline systems, the concentration of Cr in matrix and clinopyroxene rims has previously been successfully used to track magmatic evolution during eruptions (Magee et al. 2021; Ubide et al. 2023) and across eruptions (Ubide and Kamber 2018; Petrone et al. 2022). However, the competing effects of temporal and spatial heterogeneities have not been deconvoluted on the scale of a single eruption. In addition, sector zoning in clinopyroxene mantles across the paroxysms may enable tracking changes in ΔT with time by examining the difference in ^{T}Al between prism and hourglass sectors ($\Delta^{T}Al = |^{T}Al_{prism} — ^{T}Al_{hourglass}|$) as a measure of the degree of sector zoning (MacDonald et al. 2024). Therefore, we also examine the temporal and spatial variability of $\Delta^{T}Al$ in clinopyroxene mantles.

We first track the temporal variability of Cr in clinopyroxene mantles across the paroxysmal episodes included in this study. We use Cr concentrations determined by both EPMA and LA-ICP-MS (Fig. 7a), which

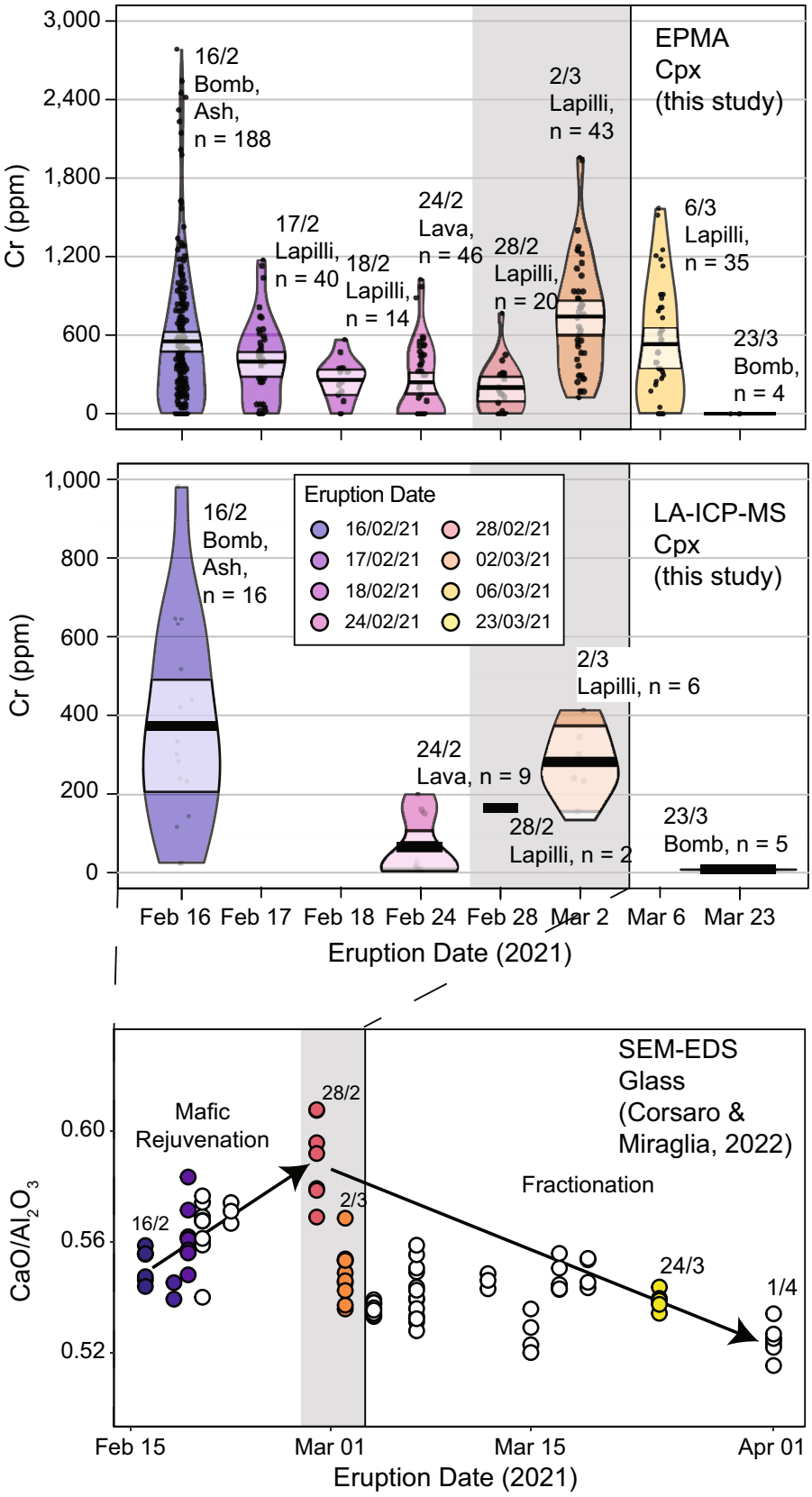

Fig. 7 **a** Pirate plots (Phillips 2017) of the distribution of Cr concentrations in clinopyroxene mantle zones (used as a proxy for melt maficity) using electron microprobe (top) and LA-ICP-MS (bottom) data. Temporal variability across the paroxysms is illustrated by the changing median values (black horizontal lines) between episodes, with a peak in maficity on 2nd March 2021. We interpret the spread of data to illustrate spatial variability, which also changes across the paroxysms. The number of analyses (n) used are indicated for each date. **b** Variations in erupted glass compositions across the paroxysms from Corsaro and Miraglia (2022), with a peak in CaO/Al_2O_3 (maficity) on the 28th February 2021, two days before the clinopyroxene maficity peak, followed by magma fractionation towards the end of the eruption. Grey vertical bars in both **a** and **b** correspond to the late February—early March peak in maficity. The dashed lines indicate time-equivalent data

complement each other as electron microprobe data are more readily available and LA-ICP-MS data provide higher precision. Although EPMA returns higher maxima than LA-ICP-MS (Fig. 7a), this may reflect the nature in which data were collected. LA-ICP-MS concentrations presented here are extracted from compositional maps by averaging pixels in a chosen area, whereas EPMA concentrations are spot analyses. In other words, LA-ICP-MS concentrations represent averages per zone, whereas EPMA concentrations may be influenced by intra-zone heterogeneities and should be treated as maximum values. Both sets of data indicate two Cr peaks: one during the first paroxysmal episode (16th February 2021) and the other partway through the series of events (2nd March 2021), after which Cr decreases until the end of the paroxysms. Using Cr as a proxy for melt evolution or maficity of the melt (i.e., where high maficity corresponds to more primitive compositions, following Ubide and Kamber 2018 and Ubide et al. 2023), our data suggests that throughout the paroxysms, the input of mafic magma peaked first during the onset of paroxysmal episodes, then waned slightly until a second peak on 2nd March 2021. Following this peak, Cr concentrations decreased until the end of the paroxysms, reflecting decreasing maficity of the melt.

The overall clinopyroxene-Cr trend is consistent with interpretations from tephra compositions from the 2021 paroxysms, where maficity and crystal fractionation were tracked using CaO/Al_2O_3 in glass (Corsaro and Miraglia 2022). In detail, the peak in glass CaO/Al_2O_3 (corresponding to the most mafic erupted composition) identified by Corsaro and Miraglia (2022) was on the 28th February, whereas Cr in our clinopyroxene peaks on 2nd March (Fig. 7). The two-day offset may be due to either 1) the effects of spatial variability on Cr enrichments in mantles (discussed below) or 2) a delay between the crystallisation of mafic mantles and their eruption. The glass compositions of Corsaro et al. (2022) also suggest that early paroxysms define a period of mafic rejuvenation, whereas clinopyroxene Cr contents show a slight evolution in composition prior to the maficity peak on the 2nd March (Fig. 7). Clinopyroxene Cr compositions obtained using high-resolution geochemical techniques may, therefore, track discrete changes in melt composition that major element analyses of glasses do not capture. Regardless, our clinopyroxene data set illustrates a decrease in melt maficity towards the end of the paroxysmal episodes, consistent with the onset of fractionation identified using glass compositions (12% crystallisation; Corsaro and Miraglia 2022). This highlights the ability of Cr enrichment in clinopyroxene to track magma evolution. Critically, decreasing maficity of erupted products may herald the end of eruptive periods, as previously observed for the 2021 La Palma eruption (Ubide et al. 2023).

Relative enrichment of ^{T}Al in prism compared to hourglass sectors of clinopyroxene mantles also varies temporally, with the highest values of $\Delta^{T}Al$ recorded during the 28th February paroxysm (Fig. 8). Interestingly, $\Delta^{T}Al$ values in late February and early March 2021 are comparable with microphenocrysts erupted during the 1974 eccentric eruption at Mt. Etna, which was characterised by vigorous mixing and fast ascent (Ubide and Kamber 2018). Clinopyroxenes erupted during the late February and early

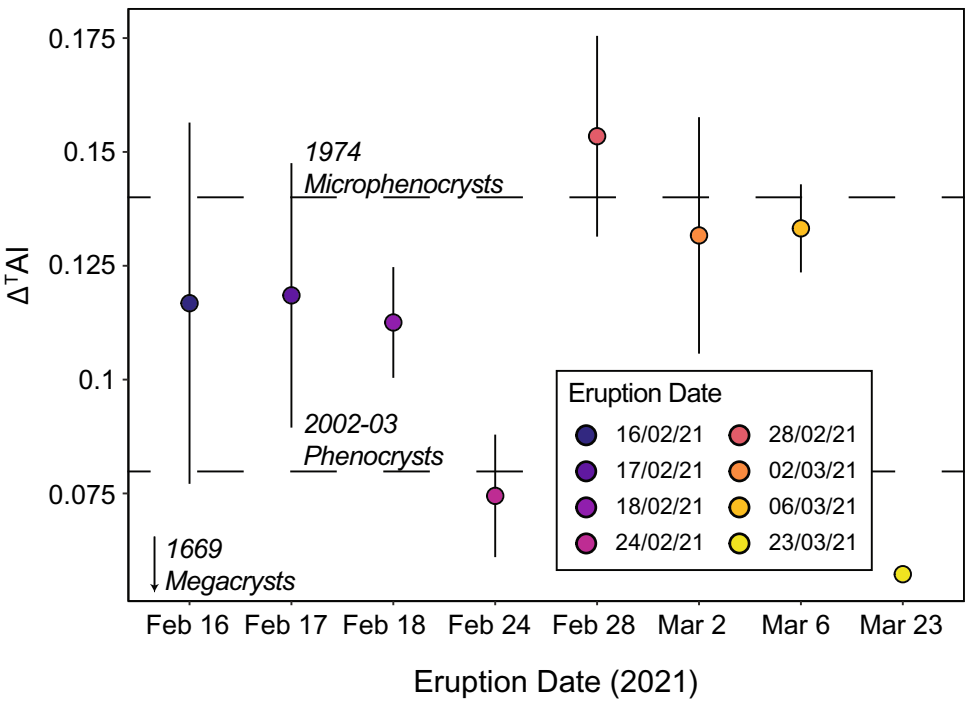

Fig. 8 Sector enrichment, measured as $\Delta^{T}Al$ ($\Delta^{T}Al = |^{T}Al_{Prism} - {}^{T}Al_{Hourglass}|$ of clinopyroxene mantles across the paroxysms. Points are average sector enrichment per sample, with error bars corresponding to 1σ. Dashed lines represent average $\Delta.^{T}Al$ from the Cr-rich mantles of clinopyroxene phenocrysts and microphenocrysts from previous eruptions as presented in MacDonald et al (2024)

March 2021 paroxysms were primarily microphenocrysts, with relatively few phenocrysts (Table S7), supporting higher ΔT than earlier paroxysms associated with initial rejuvenation and mush remobilisation. Analysis of textural complexity of clinopyroxene phenocrysts from the 2021 paroxysms by Musu et al. (2023) indicated that clinopyroxene crystals erupted during this paroxysm exhibited the least textural complexity, which the authors used to infer rapid ascent of hotter, mafic magma compared to other episodes. Our results corroborate this interpretation and suggest that mush remobilisation and the onset of magma ascent potentially occurred under conditions of higher ΔT compared to the other paroxysms.

The lowest Δ^{T}Al was recorded by clinopyroxene mantles from one of the last paroxysms (23rd March 2021; Fig. 8), which also corresponds to a decrease in maficity. Interestingly, the later paroxysms also had the longest eruptive durations, whereas the event on the 28th February had the shortest duration (Andronico et al. 2021), possibly in response to faster magma ascent rates and higher ΔT. Most of the other paroxysms have clinopyroxene with average sector enrichment comparable with historical phenocrysts, or intermediate between phenocrysts and microphenocrysts. As highlighted by MacDonald et al. (2024), sector enrichment increases with decreasing crystal size, corresponding to crystallisation under relatively high ΔT. Our results reflect this corollary and highlight changing ΔT associated with mush remobilisation and ascent throughout the paroxysms and changes in eruptive behaviour.

Cr in clinopyroxene: Spatial heterogeneity

Although the Cr concentration of clinopyroxene mantles can be used to track maficity, Cr also varies between different crystals erupted during the same event (Fig. 2). Therefore, we also explore how Cr may be affected by spatial heterogeneities. The greatest variability in Cr concentrations is observed for the 16th February and 2nd March 2021 paroxysms, based on both LA-ICP-MS and electron microprobe data (Fig. 7a; Tables S7 and S8). We note that although the number of samples (n) analysed for each paroxysm is highly variable (e.g., for EPMA, the highest quantity of data points was obtained for 28th February 2021 paroxysm, and the lowest for the final paroxysm), this in part reflects the abundance of clinopyroxene mantle zones observed during analysis. In addition, data abundance does not appear to influence data spread when comparing paroxysms with similar number of analyses (e.g., 24th February and 2nd March paroxysms; Fig. 7a). Heterogeneities in mineral populations on the sample-scale testify to complex open-system processes in magmatic plumbing systems (Wallace and Bergantz 2005; Cashman et al. 2017). Such complexities are often interpreted to reflect mush cannibalism where the dominant crystal mush is recycled by volatile-rich, hot, mafic magmas (Davidson et al. 2007; Cashman and Blundy 2013). Injection of mafic magma can effectively break up a crystal-rich mush, leading to the formation of a fluidized mixing bowl where chaotic mixing entrains crystals from different regions of the mush (Burgisser and Bergantz 2011; Bergantz et al. 2015). This results in the assembly of a heterogeneous crystal cargo that may have crystallised under different physiochemical conditions (Couch et al. 2001) and which may be resorbed to variable degrees depending on the exposure of a mineral to the invading magma (Perugini 2021), which is likely influenced by its location in the reservoir, as well as the residence time of the intruding magma (Cheng et al. 2020). Critically, in the context of the 2021 paroxysms, the greater spatial heterogeneities in clinopyroxene align with the observed maficity peaks (Fig. 7a), suggesting that periods of increased maficity enhance mush disaggregation. Between maficity peaks, heterogeneity appears to decrease with time (Fig. 7a), which may reflect the effect of longer magma residence times on crystal zoning. Numerical modelling indicates that as the new magma progressively mixes with the residence magma and mush, the proportion of crystals recording zoning increases, thus decreasing spatial variability (Cheng et al. 2020). Replenishment of mafic magma has been attributed as a critical driver of mush disaggregation, resulting in samples with complex crystal cargoes in other volcanic systems such as the East Australian hotspot track (Tapu et al. 2022), Iceland (Kahl et al. 2021), Hawaii (Kahl et al. 2023) and in arc settings (Cashman and Blundy 2013).

Along with Cr, the magnitude of Δ^{T}Al is also variable on the sample-scale, indicating that clinopyroxene mantles exhibit variable degrees of sector zoning (Fig. 8). Indeed, if the magnitude of Cr recorded by clinopyroxene mantles reflect a crystallisation environment associated with variable degrees of mixing between hotter, recharge magmas and colder, resident magmas, then it follows that the driving force for the crystallisation of mantles is mostly the change in ΔT, which in turn influences the incorporation of cations into clinopyroxene lattice sites. The greatest variability in Δ^{T}Al is typically associated with periods of increased magma input (16th February and 2nd March 2021 paroxysms, Figs. 7a and 8) and greatest variability of Cr concentration. Hence, periods of vigorous mixing associated with mafic rejuvenation result in highly variable ΔT conditions and therefore crystal sizes (phenocrysts and microphenocrysts; Table S7) and intensity of sector zoning.

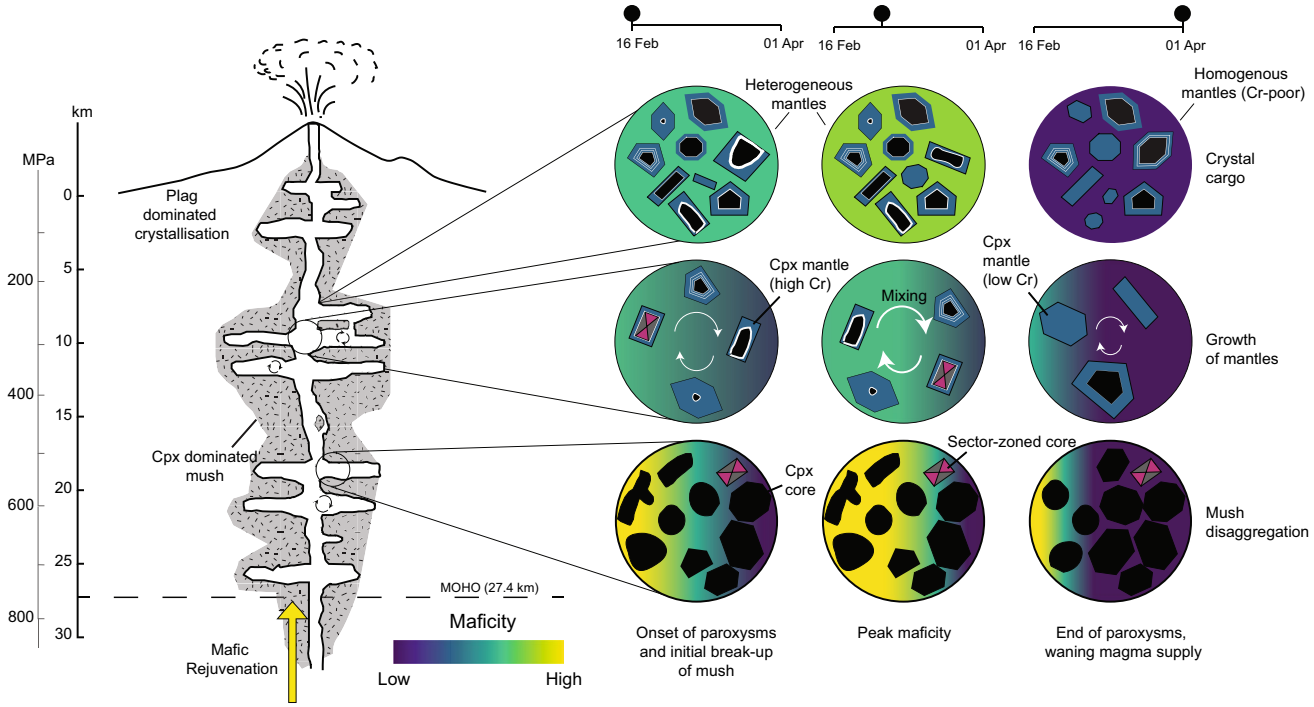

Fig. 9 Schematic representation of the plumbing system and associated magma-mush dynamics during the 2021 February–April paroxysms at Mt. Etna, Italy based on clinopyroxene composition and textures. Conversion of pressure to depth was determined following the crustal density model by Corsaro and Pompilio (2004). MOHO depth is from Hirn et al. (1997). Rejuvenation of deep mushes is driven by inputs of more mafic Cr-rich magma (yellow arrow) causing variably resorbed cores overgrown by Cr-rich mantle zones at shallower pressures, assembling a heterogeneous crystal population. Changes in mush dynamics throughout the paroxysms are represented by the inserts on the right. Black crystal zones are cores, some of which are sector-zoned. White and blue zones are mantles, with white portions representing Cr-rich bands. Thicker white bands represent higher Cr concentrations. Sector-zoned mantles are ubiquitous and so are not marked here for simplicity

Implications for magma-mush dynamics in the lead up to the 2021 paroxysms at mt. Etna

An array of geochemical, seismic, and volcanic gas data highlights the key role of mafic rejuvenation in driving the 2021 paroxysms (Bonaccorso et al. 2021; De Gori et al. 2021; Corsaro and Miraglia 2022; Mollo et al. 2022; Aiuppa et al. 2023; Giuffrida et al. 2023; Musu et al. 2023). Integrating these results with our findings, we infer that the mafic magma which fed the eruption remobilised a clinopyroxene dominated crystal mush located at approximately 530 MPa (~ 18 km depth; Figs. 6, 9). Thermodynamic modelling based on Fo content of olivine phenocrysts from the 2021 paroxysms place the origin of the intruding mafic magma at > 16 km (Giuffrida et al. 2023), corresponding well with our interpretations. Additionally, clinopyroxene cores exhibit minimal Eu anomalies (Fig. 5), attesting to the limited fractionation of plagioclase, which is commonly associated with shallower crystallisation at Mt. Etna (Giacomoni et al. 2014). The clinopyroxene cores studied here likely crystallised from a slightly evolved melt which did not initially erupt but was cogenetic to the later intruding mafic magma (Fig. 5). The input of hotter, volatile-rich mafic magma caused the cannibalisation of pre-existing mushes, as commonly documented for a variety of eruption types at Mt. Etna (Ubide and Kamber 2018; Ubide et al. 2019a), including the 2021 paroxysms (Mollo et al. 2022), which identify the intruding magma with a H_2O content > 2 wt. % (Armienti et al. 2007).

Chaotic mixing associated with mush disaggregation and remobilisation may also cause variable degrees of resorption (Perugini 2021) and overgrowth of mantles with varying Cr concentrations, reflecting the spatial variable interactions between the recharge melt and pre-existing mush. Crystallisation of mantles occurred in shallower regions of the plumbing system (281 MPa, ~ 10 km depth; Figs. 6a, 9), from which mafic magma began to ascend to shallower reservoirs (Bonaccorso et al. 2021; De Gori et al. 2021). Our results indicate that this process was most significant for the first paroxysm, where the initial pulse of mafic magma caused a greater degree of mush disaggregation, mixing and undercooling which resulted in the crystallisation of mantles which record both variable Cr concentrations and sector enrichment

(Figs. 7a and 8). This dynamic environment produced a highly heterogeneous crystal cargo, which then ascended to the shallower magmatic reservoirs. Clinopyroxene rims crystallised during ascent through the central conduit system of the volcano, mostly prior to plagioclase (Fig. 9) considering the limited Eu anomalies (Fig. 5). Shallow storage is supported by seismicity and strain monitoring data, which indicate that the South-East Crater is fed from a reservoir as shallow as 0.5–1 km depth (Bonaccorso et al. 2021; De Gori et al. 2021), where the final ejection of magma is likely controlled by volatile accumulation (Behncke et al. 2014).

Mush disaggregation and remobilisation proceeded until the maficity peak part way through the eruption, after which maficity decreased during the final month of the paroxysms (Fig. 7). Decreasing maficity could be attributed to either mixing with a more evolved melt composition, or to cooling and fractional crystallisation of the resident magma, potentially due to waning magma supply as observed two weeks before the end of the 2021 La Palma eruption in the Canary Islands (Ubide et al. 2023). Previous glass and mineral compositional data together with mass balance calculations from the 2021 Mt. Etna paroxysms suggest that the geochemical inflection was due to fractional crystallisation (Corsaro and Miraglia 2022; Musu et al. 2023). In addition, syn-eruptive observations noted that the paroxysm on the 28th February produced the highest lava fountain and had the shortest eruption duration (Andronico et al. 2021), which suggest faster ascent rates and less viscous (i.e., more mafic) magma compositions (La Spina et al. 2021; Musu et al. 2023). After this peak, eruption duration increased (Andronico et al. 2021) and erupted products became increasingly more evolved consistent with waning magma supply (Fig. 7b; Corsaro and Miraglia 2022; Musu et al. 2023). Interestingly, SO_2 gas measurements do not appear to reflect changes in magma composition (Aiuppa et al. 2023), highlighting the subtlety of melt compositional variations and the critical role of petrological monitoring to detect them. The interpretation of decreasing supply of mafic magma is consistent with clinopyroxene mantles with lower Cr concentrations (Fig. 7a), in minor disequilibrium with recycled cores which therefore preserved euhedral habits. We postulate that waning magma supply caused less efficient mush remobilisation, ultimately resulting in lower degrees of magma mixing and limiting the assembly of heterogeneous crystal populations. Following this reasoning, lower sector enrichments in mantles associated with the final paroxysms are consistent with more sluggish mush remobilisation (Fig. 8) and slower ascent rates due to decreased maficity and increased viscosity (La Spina et al. 2021).

Overall, the spatial and temporal variability of Cr enrichments in clinopyroxene and the development of sector zoning may help to better understand the role played by complex magma-mush dynamics in the lead up to paroxysmal eruptions. Our results support the notion that erupted products at Mt. Etna entrain a significant proportion of mush-derived crystals which formed from earlier batches of cogenetic magma, and that phenocryst-rich bulk rock compositions do not accurately reflect true melt compositions (Magee et al. 2021; Ubide et al. 2022). Importantly, waning magma supply causes less efficient mush remobilisation and may herald the end of an eruptive period. The integration of clinopyroxene data with other petrological monitoring approaches show promise at Mt. Etna (Ubide and Kamber 2018; Corsaro and Miraglia 2022) and other basaltic volcanoes (Petrone et al. 2022; Ubide et al. 2023). Waning magma supply during the La Palma 2021 eruption and the 2021 Mt. Etna paroxysms both occurred on the time scale of weeks, highlighting the importance of petrological monitoring for eruption forecasting at basaltic volcanoes. Further clinopyroxene compositional variability from distinct ascent pathways (e.g., eccentric eruptions, which bypass the central conduit system; Corsaro et al. 2009), eruption styles and volcanic settings may further illuminate the complexity of magma-mush dynamics across the structure of plumbing systems in basaltic volcanoes.

Conclusions

Using a combination of high-resolution analytical techniques, we have explored how clinopyroxene may record temporal and spatial variations across the February–April 2021 paroxysmal episodes at Mt. Etna, Italy. Our results indicate that Cr enrichments associated with eruption-triggering mafic rejuvenation vary in clinopyroxene crystals, reflecting temporal variations linked to the supply of fresh, mafic magma into the plumbing system, and spatial variations associated with the chaotic nature of mush remobilisation, mixing and ascent. Clinopyroxene cores, cannibalised from deep mushes located in the lower crust ($P = 534 \pm 46$ MPa; average ± standard deviation; ~ 18 km depth), exhibit a spectrum of resorption textures, indicative of increasing degrees of crystal-melt reactions and disequilibrium associated with their remobilisation. Mantles formed from the replenishing magmas in the mid crust (281 ± 53 MPa; ~ 10 km depth), recording variations in magma supply with time. Rims are Cr-poor, have compositions intermediate between cores and mantles and are interpreted to form upon ascent from a mixed magma composition.

The composition of clinopyroxene mantles represents an important archive of mush dynamics and its variations through time, as: (1) increasing Cr concentrations correlate with new inputs of magma; (2) the spread in Cr concentrations serve as an indication of the degree of mush

disaggregation and magma flux, and (3) the extent of sector zoning reflects magma undercooling modulated by mixing. Together, decreasing Cr concentrations, Cr variability and sector enrichment herald the end of the eruptive period over a timescale of weeks, which may be valuable in monitoring the end of future eruptions in mafic alkaline systems.

Our data highlight not only the effectiveness of clinopyroxene as a record of both temporal trends in magma composition and spatial variability in mush reservoirs, but also the effectiveness of combining high-resolution analytical techniques, such as thin section scale X-ray fluorescence microscopy with quantitative LA-ICP-MS trace element mapping, to identify sample-scale heterogeneities and magma dynamics throughout volcanic eruptions.

Supplementary Information The online version contains supplementary material available at https://doi.org/10.1007/s00410-024-02174-5.

Acknowledgements This work was supported by a Foundation Research Excellence Award from The University of Queensland, the Advance Queensland Women's Research Assistance Program from the Queensland Government, and an Australian Research Council Discovery Project to T.U. (UQ-FREA RM2019001828, WRAP109-2019RD1 RM2020002371, ARC DP200101566). A.M. was supported by the Australian Government Research Training Program (RTP; PhD scholarship) for the duration of this study. T.U. was supported by an Australian Research Council Future Fellowship (ARC FT230100230). S.M. acknowledges the funding from MIUR-PRIN 2022 PROVES Project (Grant #2022N4FBAA). This publication includes work carried out at INGV-RM1 facilities with the support of EXCITE – EC- HORIZON 2020 -INFRAIA 2020 Integrating Activities for Starting Communities Trans-National Access action under grant agreement N.101005611. X-ray fluorescence microscopy mapping was undertaken on the XFM beamline at the Australian Synchrotron, part of ANSTO (experiment: AS221/XFM/18100). We would like to thank Daryl Howard for assistance operating the beamline and David Murphy for help and discussion during analysis. We would also like to thank Henrietta Cathey, Al-Tamini Tapu and Manuela Nazzari for assistance with microprobe analysis. We acknowledge the facilities and staff of the Australian Microscopy & Microanalysis Research Facility at the Centre for Microscopy and Microanalysis (CMM), The University of Queensland. We warmly thank Salvatore and Graziella Ragonesi for carefully collecting the 60x series of tephra samples. We thank Jon Blundy and Penny Wieser for their insightful comments and suggestions on a preliminary draft. David Neave, Felix Marxer and an anonymous reviewer are acknowledged for their helpful and constructive comments which improved the discussion of our results. We are grateful to the editorial guidance provided by Ralf Dohmen.

Funding Open Access funding enabled and organized by CAUL and its Member Institutions. University of Queensland, UQ-FREA RM2019001828, Teresa Ubide, Queensland Government, WRAP109-2019RD1 RM2020002371, Teresa Ubide, Australian Research Council, ARC DP200101566, Teresa Ubide, Horizon 2020, N.101005611, Alice Macdonald.

Data availability All data used in this study are provided in the supplementary material.

Declarations

Conflict of interest The authors have no competing interests to declare that are relevant to the content of this article.

References

Aiuppa A, Lo Bue TG, Alparone S, Bitetto M, Coltelli M, Delle Donne D, Ganci G, Pecora E (2023) A SO2 flux study of the Etna volcano 2020–2021 paroxysmal sequences. Front Earth Sci 11:1115111

Andronico D, Cannata A, Di Grazia G, Ferrari F (2021) The 1986–2021 paroxysmal episodes at the summit craters of Mt. Etna: insights into volcano dynamics and hazard. Earth-Sci Rev 220:103686

Arculus RJ (1978) Mineralogy and petrology of Grenada, Lesser Antilles island arc. Contrib Miner Petrol 65:413–424

Armienti P, Tonarini S, Innocenti F, Orazio DM (2007) Mount Etna pyroxene as tracer of petrogenetic processes and dynamics of the feeding system. Cenozoic Volcanism in the Mediterranean, Geol Soc Am Spec Papers 418:265

Arzilli F, Polacci M, La Spina G, Le Gall N, Llewellin EW, Brooker RA, Torres-Orozco R, Di Genova D, Neave DA, Hartley ME, Mader HM (2022) Dendiritic crystallization in hydrous basaltic magmas controls magma mobility within the Earth's crust. Nat Commun 13:3354

Barnes SJ, Paterson D, Ubide T, Schoneveld LE, Ryan C, Le Vaillant M (2020) Imaging trace-element zoning in pyroxenes using synchrotron xrf mapping with the maia detector array: benefit of low-incident energy. Am Mineral: J Earth Planetary Mater 105:136–140

Batki A, Pál-Molnár E, Jankovics MÉ, Kerr AC, Kiss B, Markl G, Heincz A, Harangi S (2018) Insights into the evolution of an alkaline magmatic system: an in situ trace element study of clinopyroxenes from the ditrău alkaline massif, romania. Lithos 300:51–71

Behncke B, Branca S, Corsaro RA, De Beni E, Miraglia L, Proietti C (2014) The 2011–2012 summit activity of Mount Etna: birth, growth and products of the new se crater. J Volcanol Geoth Res 270:10–21

Bergantz G, Schleicher J, Burgisser A (2015) Open-system dynamics and mixing in magma mushes. Nat Geosci 8:793–796

Blundy JD, Falloon TJ, Wood BJ, Dalton JA (1995) Sodium partitioning between clinopyroxene and silicate melts. J Geophys Res: Solid Earth 100:15501–15515

Blundy J, Robinson J, Wood B (1998) Heavy REE are compatible in clinopyroxene on the spinel lherzolite solidus. Earth Planet Sci Lett 160:493–504

Bonaccorso A, Carleo L, Currenti G, Sicali A (2021) Magma migration at shallower levels and lava fountains sequence as revealed by borehole dilatometers on Etna volcano. Front Earth Sci 9:740505

Burgisser A, Bergantz GW (2011) A rapid mechanism to remobilize and homogenize highly crystalline magma bodies. Nature 471:212–215

Cashman K, Blundy J (2013) Petrological cannibalism: the chemical and textural consequences of incremental magma body growth. Contrib Miner Petrol 166:703–729

Cashman KV, Sparks RSJ, Blundy JD (2017) Vertically extensive and unstable magmatic systems: a unified view of igneous processes. Science 355:eaag3055

Cheng L, Costa F, Bergantz G (2020) Linking fluid dynamics and olivine crystal scale zoning during simulated magma intrusion. Contrib Miner Petrol 175:53

Cooper KM, Kent AJ (2014) Rapid remobilization of magmatic crystals kept in cold storage. Nature 506:480–483

Corsaro RA, Miraglia L (2022) Near real-time petrologic monitoring on volcanic glass to infer magmatic processes during the February–April 2021 paroxysms of the south-east crater Etna. Front Earth Sci 10:828026

Corsaro RA, Pompilio M (2004) Buoyancy-controlled eruption of magmas at Mt Etna. Terra Nova 16:16–22

Corsaro R, Métrich N, Allard P, Andronico D, Miraglia L, Fourmentraux C (2009) The 1974 flank eruption of Mount Etna: an archetype for deep dike-fed eruptions at basaltic volcanoes and a milestone in Etna's recent history. J Geophys Res Solid Earth 114:B7

Couch S, Sparks R, Carroll M (2001) Mineral disequilibrium in lavas explained by convective self-mixing in open magma chambers. Nature 411:1037–1039

Davidson J, Morgan D, Charlier B, Harlou R, Hora J (2007) Microsampling and isotopic analysis of igneous rocks: Implications for the study of magmatic systems. Annu Rev Earth Planet Sci 35:273–311

De Gori P, Giampiccolo E, Cocina O, Branca S, Doglioni C, Chiarabba C (2021) Re-pressurized magma at Mt. Etna, Italy, may feed eruptions for years. Commun Earth Environ 2:1–9

Di Stefano F, Mollo S, Ubide T, Petrone CM, Caulfield J, Scarlato P, Nazzari M, Andronico D, Del Bello E (2020) Mush cannibalism and disruption recorded by clinopyroxene phenocrysts at Stromboli volcano: new insights from recent 2003–2017 activity. Lithos 360:105440

D'Orazio M, Armienti P, Cerretini S (1998) Phenocryst/matrix trace-element partition coefficients for hawaiite-trachyte lavas from the Ellittico volcanic sequence (Mt. Etna, Sicily, Italy). Mineral Petrol 64(1–4):65

Edmonds M, Cashman KV, Holness M, Jackson M (2019) Architecture and dynamics of magma reservoirs. Phil Trans R Soc A 377:20180298

Gansecki C, Lee RL, Shea T, Lundblad SP, Hon K, Parcheta C (2019) The tangled tale of Kīlauea's 2018 eruption as told by geochemical monitoring. Science 366:eaaz0147

Giacomoni PP, Ferlito C, Coltorti M, Bonadiman C, Lanzafame G (2014) Plagioclase as archive of magma ascent dynamics on "open conduit" volcanoes: the 2001–2006 eruptive period at Mt. Etna Earth-Science Reviews 138:371–393

Giacomoni PP, Coltorti M, Bryce J, Fahnestock M, Guitreau M (2016) Mt. Etna plumbing system revealed by combined textural, compositional, and thermobarometric studies in clinopyroxenes. Contrib Mineral Petrol 171:34

Giuffrida M, Cardone M, Zuccarello F, Viccaro M (2023) Etna 2011–2022: discoveries from a decade of activity at the volcano. Earth Sci Rev 245:104563

Grove TL, Juster TC (1989) Experimental investigations of low-Ca pyroxene stability and olivine-pyroxene-liquid equilibria at 1-atm in natural basaltic and andesitic liquids. Contrib Miner Petrol 103:287–305

Hammer J, Jacob S, Welsch B, Hellebrand E, Sinton J (2016) Clinopyroxene in postshield Haleakala ankaramite: 1. Efficacy of thermobarometry. Contrib Miner Petrol 171:1–23

Hekinian R, Thompson G (1976) Comparative geochemistry of volcanics from rift valleys, transform faults and aseismic ridges. Contrib Miner Petrol 57:145–162

Hill E, Wood BJ, Blundy JD (2000) The effect of Ca-Tschermaks component on trace element partitioning between clinopyroxene and silicate melt. Lithos 53:203–215

Hirn A, Nicolich R, Gallart J, Laigle M, Cernobori L, Group ES (1997) Roots of Etna volcano in faults of great earthquakes. Earth Planetary Sci Lett 148:171–191

Jarosewich E, Nelen J, Norberg JA (1980) Reference samples for electron microprobe analysis. Geostand Newsl 4:43–47

Jorgenson C, Higgins O, Petrelli M, Bégué F, Caricchi L (2022) A machine learning based approach to clinopyroxene thermobarometry: Model optimisation and distribution for use in earth sciences. J Geophys Res: Solid Earth 127:e2021JB022904

Kahl M, Chakraborty S, Costa F, Pompilio M, Liuzzo M, Viccaro M (2013) Compositionally zoned crystals and real-time degassing data reveal changes in magma transfer dynamics during the 2006 summit eruptive episodes of Mt. Etna Bull Volcanol 75:1–14

Kahl M, Bali E, Guðfinnsson GH, Neave DA, Ubide T, van der Meer QHA, Matthew S (2021) Conditions and dynamics of magma storage in the snæfellsnes volcanic zone, western iceland: insights from the Bu´ðahraun and berserkjahraun eruptions. J Petrol 62:1–29

Kahl M, Morgan DJ, Thornber C, Walshaw R, Lynn KJ, Trusdell FA (2023) Dynamics of magma mixing and magma mobilisation beneath Mauna Loa—insights from the 1950 AD Southwest Rift Zone eruption. Bull Volcanol 85:75

Kent AJ, Till CB, Cooper KM (2023) Start me up: the relationship between volcanic eruption characteristics and eruption initiation mechanisms. Volcanica 6:161–172

Kouchi A, Sugawara Y, Kashima K, Sunagawa I (1983) Laboratory growth of sector zoned clinopyroxenes in the system CaMgSi2O6-CaTiAl2O6. Contrib Miner Petrol 83:177–184

La Spina G, Arzilli F, Llewellin E, Burton M, Clarke AB, Vitturi MDM, Polacci M, Hartley M, Di Genova D, Mader H (2021) Explosivity of basaltic lava fountains is controlled by magma rheology, ascent rate and outgassing. Earth Planet Sci Lett 553:116658

Li X, Zeng Z, Yang H, Zhao Y, Yin X, Wang X, Chen S, Qi H, Guo K (2020) Integrated major and trace element study of clinopyroxene in basic, intermediate and acidic volcanic rocks from the middle Okinawa trough: Insights into petrogenesis and the influence of subduction component. Lithos 352:105320

MacDonald A, Ubide T, Mollo S, Masotta M, Pontesilli A (2022) Trace element partitioning in zoned clinopyroxene as a proxy for undercooling: experimental constraints from trachybasaltic magmas. Geochim Cosmochim Acta 336:249–268

MacDonald A, Ubide T, Mollo S, Pontesilli A, Masotta M (2023) The influence of undercooling and sector zoning on clinopyroxene–melt equilibrium and thermobarometry. J Petrol 64:egad074

MacDonald A, Ubide T, Mollo S (2024) Degree of sector zoning in clinopyroxene records dynamic magma recharge and ascent. Geochim Cosmochim Acta 378:245–258

Magee R, Ubide T, Kahl M (2020) The lead-up to Mount Etna's most destructive historic eruption (1669). Cryptic recharge recorded in clinopyroxene. J Petrol 61:025

Magee R, Ubide T, Caulfield J (2021) Days to weeks of syn-eruptive magma interaction: High-resolution geochemistry of the

2002–03 branched eruption at Mount Etna. Earth Planet Sci Lett 565:116904
Mangler MF, Petrone CM, Hill S, Delgado-Granados H, Prytulak J (2020) A pyroxenic view on magma hybridization and crystallization at Popocatépetl volcano, Mexico. Front Earth Sci 8:362
Masotta M, Pontesilli A, Mollo S, Armienti P, Ubide T, Nazzari M, Scarlato P (2020) The role of undercooling during clinopyroxene growth in trachybasaltic magmas: insights on magma decompression and cooling at Mt. Etna Volcano Geochimica Et Cosmochimica Acta 268:258–276
Mcdonough WF, Sun S-S (1995) The composition of the earth. Chem Geol 120:223–253
Métrich N, Rutherford MJ (1998) Low pressure crystallization paths of H2O-saturated basaltic-hawaiitic melts from Mt Etna: implications for open-system degassing of basaltic volcanoes. Geochim Cosmochim Acta 62:1195–1205
Mollo S, Del Gaudio P, Ventura G, Iezzi G, Scarlato P (2010) Dependence of clinopyroxene composition on cooling rate in basaltic magmas: Implications for thermobarometry. Lithos 118:302–312
Mollo S, Blundy J, Iezzi G, Scarlato P, Langone A (2013) The partitioning of trace elements between clinopyroxene and trachybasaltic melt during rapid cooling and crystal growth. Contrib Miner Petrol 166:1633–1654
Mollo S, Putirka K, Misiti V, Soligo M, Scarlato P (2013) A new test for equilibrium based on clinopyroxene–melt pairs: clues on the solidification temperatures of etnean alkaline melts at post-eruptive conditions. Chem Geol 352:92–100
Mollo S, Giacomoni P, Andronico D, Scarlato P (2015) Clinopyroxene and titanomagnetite cation redistributions at Mt. Etna volcano (Sicily, Italy): footprints of the final solidification history of lava fountains and lava flows. Chem Geol 406:45–54
Mollo S, Giacomoni PP, Coltorti M, Ferlito C, Iezzi G, Scarlato P (2015) Reconstruction of magmatic variables governing recent etnean eruptions: constraints from mineral chemistry and P-T–fo2–H2O modeling. Lithos 212:311–320
Mollo S, Blundy J, Scarlato P, De Cristofaro SP, Tecchiato V, Di Stefano F, Vetere F, Holtz F, Bachmann O (2018) An integrated PT-H2O-lattice strain model to quantify the role of clinopyroxene fractionation on REE+ Y and HFSE patterns of mafic alkaline magmas: application to eruptions at Mt. Etna Earth-Sci Rev 185:32–56
Mollo S, Ubide T, Di Stefano F, Nazzari M, Scarlato P (2020) Polybaric/polythermal magma transport and trace element partitioning recorded in single crystals: a case study of a zoned clinopyroxene from Mt. Etna Lithos 356:105382
Mollo S, Pontesilli A, Moschini P, Palummo F, Taddeucci J, Andronico D, Del Bello E, Scarlato P (2022) Modeling the crystallization conditions of clinopyroxene crystals erupted during February–April 2021 lava fountains at Mt. Etna: implications for the dynamic transfer of magmas. Lithos 420:106710
Mollo S, Moschini P, Ubide T, MacDonald A, Vetere F, Nazzari M, Misiti V, Miyajima N, Melai C, Di Genova D, Vona A, Di Fiore F, Romano C (2023) Kinetic partitioning of trace cations between zoned clinopyroxene and a variably cooled-decompressed alkali basalt: thermodynamic considerations on lattice strain and electrostatic energies of substitution. Geochim Cosmochim Acta 361:40–66
Müller T, Dohmen R, Becker H, Ter Heege JH, Chakraborty S (2013) Fe–Mg interdiffusion rates in clinopyroxene: experimental data and implications for Fe–Mg exchange geothermometers. Contrib Miner Petrol 166:1563–1576
Murru M, Montuori C, Wyss M, Privitera E (1999) The locations of magma chambers at Mt. Etna, Italy, mapped by b-values. Geophys Res Lett 26:2553–2556
Musu A, Corsaro RA, Higgins O, Jorgenson C, Petrelli M, Caricchi L (2023) The magmatic evolution of south-east crater (Mt. Etna) during the February–April 2021 sequence of lava fountains from a mineral chemistry perspective. Bull Volcanol 85:33
Nachar N (2008) The mann-whitney u: a test for assessing whether two independent samples come from the same distribution. Tutor Quant Methods Psychol 4:13–20
Neave DA, Putirka KD (2017) A new clinopyroxene-liquid barometer, and implications for magma storage pressures under Icelandic rift zones. Am Miner 102:777–794
Nimis P (1995) A clinopyroxene geobarometer for basaltic systems based on crystal-structure modeling. Contrib Miner Petrol 121:115–125
Paton C, Hellstrom J, Paul B, Woodhead J, Hergt J (2011) Iolite: freeware for the visualisation and processing of mass spectrometric data. J Anal at Spectrom 26:2508–2518
Perinelli C, Mollo S, Gaeta M, De Cristofaro SP, Palladino DM, Armienti P, Scarlato P, Putirka KD (2016) An improved clinopyroxene-based hygrometer for etnean magmas and implications for eruption triggering mechanisms. Am Miner 101:2774–2777
Perugini D (2021) The fingerprint of magma mixing in minerals. In: The mixing of magmas: field evidence, numerical models, experiments, 1st edn. Springer, pp 113–126
Petrone CM, Mollo S, Gertisser R, Buret Y, Scarlato P, Del Bello E, Andronico D, Ellis B, Pontesilli A, De Astis G (2022) Magma recharge and mush rejuvenation drive paroxysmal activity at stromboli volcano. Nat Commun 13:7717
Phillips ND (2017) Yarrr! The pirate's guide to r. APS Observer 30:22–23
Putirka K (1999) Clinopyroxene+ liquid equilibria to 100 kbar and 2450 k. Contrib Miner Petrol 135:151–163
Putirka KD (2008) Thermometers and barometers for volcanic systems. Rev Mineral Geochem 69:61–120
Putirka KD, Mikaelian H, Ryerson F, Shaw H (2003) New clinopyroxene-liquid thermobarometers for mafic, evolved, and volatile-bearing lava compositions, with applications to lavas from Tibet and the snake river plain, Idaho. Am Miner 88:1542–1554
Scaillet B, Holtz F, Pichavant M (2016) Experimental constraints on the formation of silicic magmas. Elements 12:109–114
Sparks R, Annen C, Blundy J, Cashman K, Rust A, Jackson M (2019) Formation and dynamics of magma reservoirs. Philosophical Trans Royal Soc A 377:20180019
Streck MJ (2008) Mineral textures and zoning as evidence for open system processes. Rev Mineral Geochem 69:595–622
Tapu A, Ubide T, Vasconcelos P (2022) Plumbing system architecture of late-stage hotspot volcanoes in eastern Australia. J Petrol 63:015
Ubide T, Kamber BS (2018) Volcanic crystals as time capsules of eruption history. Nat Commun 9:1–12
Ubide T, Mollo S, Zhao J-X, Nazzari M, Scarlato P (2019) Sector-zoned clinopyroxene as a recorder of magma history, eruption triggers, and ascent rates. Geochim Cosmochim Acta 251:265–283
Ubide T, Caulfield J, Brandt C, Bussweiler Y, Mollo S, Di Stefano F, Nazzari M, Scarlato P (2019) Deep magma storage revealed by multi-method elemental mapping of clinopyroxene megacrysts at Stromboli volcano. Front Earth Sci 7:239
Ubide T, Larrea P, Becerril L, Galé C (2022) Volcanic plumbing filters on ocean-island basalt geochemistry. Geology 50:26–31
Ubide T, Márquez Á, Ancochea E, Huertas MJ, Herrera R, Coello-Bravo JJ, Sanz-Mangas D, Mulder J, Macdonald A, Galindo I (2023) Discrete magma injections drive the 2021 La Palma eruption. Science Advances 9:eadg4813
Van Orman JA, Grove TL, Shimizu N (2001) Rare earth element diffusion in diopside: influence of temperature, pressure, and

ionic radius, and an elastic model for diffusion in silicates. Contrib Miner Petrol 141:687–703
Wallace GS, Bergantz GW (2005) Reconciling heterogeneity in crystal zoning data: an application of shared characteristic diagrams at chaos crags, lassen volcanic center, California. Contrib Miner Petrol 149:98–112
Wass SY (1979) Multiple origins of clinopyroxenes in alkali basaltic rocks. Lithos 12:113–132
Wieser P, Petrelli M, Lubbers J, Wieser E, Kent AJ, Till C (2022) Thermobar: an open-source python3 tool for thermobarometry and hygrometry. Volcanica 5:349–384
Wood BJ, Blundy JD (2001) The effect of cation charge on crystal–melt partitioning of trace elements. Earth Planet Sci Lett 188:59–71
Zhang Y, Ni H, Chen Y (2010) Diffusion data in silicate melts. Rev Mineral Geochem 72:311–408